Fuel xxx (xxxx) xxx

Contents lists available at ScienceDirect

Fuel

journal homepage: www.elsevier.com/locate/fuel

Full Length Article

Surface tension and evaporation behavior of liquid fuel droplets at transcritical conditions: Towards bridging the gap between molecular dynamics and continuum simulations

Prajesh Jangale, Ehsan Hosseini, Mohammad Zakertabrizi, Dorrin Jarrahbashi *

J. Mike Walker '66 Mechanical Engineering Department, Texas A&M University, College Station, TX 77843, USA

ARTICLE INFO

Keywords:
Droplet evaporation
Surface tension
Transcritical conditions
Molecular dynamics

ABSTRACT

The phase transition from subcritical to supercritical conditions, referred to as transcritical behavior, significantly impacts the evaporation and fuel–air mixing in high-pressure liquid-fuel propulsion systems. Transcritical behavior is characterized as a transition from classical two-phase evaporation to a single-phase gas-like diffusion regime as surface tension and latent heat of vaporization reduce. However, the interfacial behavior represented by the surface tension coefficient and evaporation rate during this transition which are crucial inputs for Computational Fluid Dynamics (CFD) simulations of practical transcritical fuel spray is still missing. This study aims at developing new evaporation rate and surface tension models for transcritical *n*-dodecane droplets using molecular dynamics (MD) simulations irrespective of the droplet size. As MD simulations are primarily limited to the nanoscale, the new models can bridge the gap between MD and continuum simulations and enable the direct application of these findings to microscopic droplets. A new characteristic timescale, i.e., "undroplet time," is defined which marks the transition from classical two-phase evaporation to single-phase gas-like diffusion behavior. The undroplet time indicates the onset of droplet core disintegration and penetration of nitrogen molecules into the droplet, which occurs after the vanishment of the surface tension. By normalizing the time with respect to the undroplet time, the rate of surface tension decay, evaporation rate, and the rate of droplet mass depletion become independent of the droplet size. Calculation of pairwise correlation coefficients for the entire MD results shows that both surface tension coefficient and evaporation rate are strongly correlated with the background temperature, while pressure and droplet size play a less significant role past the critical point. Therefore, new models for surface tension coefficient and evaporation rate spanning from sub- to supercritical conditions are developed as a function of background pressure and temperature, which can be used in continuum simulations. The identified phase change behavior based on the undroplet time shows a good agreement with the phase change regime maps obtained using microscale experiments and nanoscale MD predictions.

1. Introduction

Liquid jet breakup and the breakup and evaporation of the resultant droplets into much smaller droplets, are fundamental phenomena governing mixing and combustion in modern propulsion and energy conversion systems operating at high pressures, e.g., liquid rockets [1–14], reciprocating engines [15,16], scramjets [17,18], gas turbines [19], and supercritical power generation cycles [20,21]. The design of current and future liquid-fueled propulsion systems is shifting toward much higher combustor pressures that can exceed the nominal critical pressure of the fuel and air, known as supercritical conditions [22]. In high-pressure combustors, the liquid fuel, initially at subcritical temperatures, is injected into the ambient air at supercritical pressure and temperature resulting in fuel temperature exceeding its nominal critical point. The transition of the fuel from subcritical to supercritical temperature, referred to as "transcritical behavior," is identified as the transition from a liquid-like (LL) into a gas-like (GL) behavior by crossing the pseudo-boiling (Widom) line on the phase diagram as illustrated in Fig. 1 [23,24]. Transcritical behavior, which has been the subject of controversy in the past decades [25,26], is associated with a significant change in thermophysical behavior, including a sharp decrease in fuel density and surface tension and a spike in specific heat past the pseudo-boiling

---

* Corresponding author.
E-mail address: djarrahbashi@tamu.edu (D. Jarrahbashi).

https://doi.org/10.1016/j.fuel.2023.130187
Received 9 August 2023; Received in revised form 12 October 2023; Accepted 24 October 2023

Please cite this article as: Prajesh Jangale et al., *Fuel*, https://doi.org/10.1016/j.fuel.2023.130187

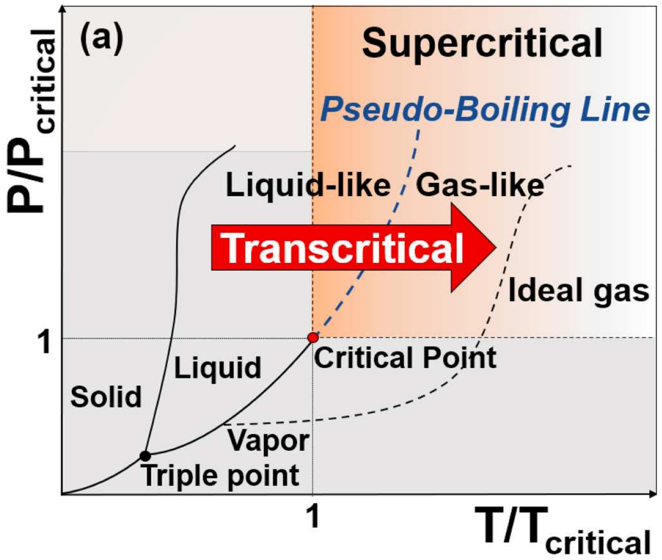

Fig. 1. Phase diagram showing transcritical behavior in a multicomponent system by transitioning from a liquid-like (LL) to a gas-like (GL) state by crossing the pseudo-boiling (Widom) line at supercritical pressures.

line. The shift in properties from subcritical to supercritical conditions imposes a drastic change in the mixing and evaporation behavior of fuel droplets, as demonstrated in several experimental investigations [27–30]. The liquid fuel jet transitions from a two-phase regime dominated by surface tension effects with a sharp liquid/gas interface known as "classical atomization" [31] into a single-phase regime governed by GL diffusion in the absence of surface tension effects. Transitioning to a GL diffusion regime and eliminating liquid fuel droplets can significantly enhance fuel–air mixing [16,32–34]. Although subcritical two-phase breakup [35] and single-phase supercritical mixing [5] are better understood, transcritical breakup have remained elusive. Crua et al. [36] performed high-speed, long-distance microscopy to capture the transcritical behavior for three single-component fuel sprays (*n*-heptane, *n*-dodecane, *n*-hexadecane), injected into the mixture of gases at temperatures (700–1200 K) and pressures (2–11 MPa) exceeding the nominal critical point of these fuels. These measurements were taken after the end of the injection, where the lower flow speeds allowed the resolution of isolated microscopic droplets that remained in the combustion chamber before the start of the second injection. Microscopic images demonstrated that the droplets retained their spherical shape even at supercritical conditions and reduced in size under the influence of surface tension similar to evaporation behavior at subcritical conditions. This is clear evidence that surface tension effects are present at supercritical conditions, in contrast to pure single-component systems, e.g., nitrogen injected into nitrogen at supercritical conditions [37], where surface tension vanishes past the critical point. These experiments [36] also indicated that it takes a few milliseconds for a microscopic droplet exposed to supercritical conditions to be heated to the critical temperature, after which the droplet turns into a GL fluid. While the fuel spray length can exceed a few centimeters, droplet diameters remain within a few microns. Such large-scale disparities hinder experimental diagnostics at high-pressure and higher flow speeds. Due to insufficient optical diagnostics, these results were captured at a much lower flow speed than a developing spray that more accurately reflects fuel–air mixing in the combustor.

Consistent with the experiments in microscopic transcritical droplets [36], MD simulations [16,25,26,30,36,38–44] and linear gradient theory (LGT) [25,26,42,45,46] have shown that surface tension forces persist at transcritical conditions and decay as the interfacial temperature increases. MD simulations can provide the changes in surface tension and thermophysical properties at transcritical conditions without any predetermined assumptions [47,48]; however, these studies are limited to nanoscale due to their high computational costs. Computational Fluid Dynamics (CFD) simulations require input interfacial properties such as surface tension and mass transport coefficients to accurately predict liquid fuel sprays at transcritical conditions. The lack of appropriate computational tools capable of translating interfacial behavior to higher scales of interest to engineering applications is another obstacle in resolving transcritical breakup [30,49–51]. Despite limited studies [52,53], several studies have neglected surface tension effects entirely in CFD modeling of transcritical jets/droplets by assuming surface tension effects are not significant above the critical point in contrast to mere evidence of surface tension persistence at transcritical conditions [54–60]. Moreover, for a droplet undergoing a transition from subcritical to supercritical conditions, the traditional d^2-law for droplet evaporation is violated, and studies [24,36,61] have shown a dramatic changes in droplet size which is linked to the transition to a single-phase GL diffusion, also known as supercritical GL mixing. Thus, there is a need for theoretical models to accurately represent the variation in surface tension and evaporation behavior at transcritical conditions for CFD simulations. Particularly, in classical Eulerian-Lagrangian simulations of fuel sprays, the interactions between the continuous Eulerian gas phase and the Lagrangian droplet phase are governed by implementing sub-models, e.g., breakup and evaporation models. The existing breakup sub-models, e.g., Kelvin-Helmholtz Rayleigh-Taylor (KH-RT) breakup model, Stochastic Secondary Droplet model (SSD), Discrete Phase Model are commonly used for subcritical droplet and their applicability for transcritical conditions has not been proved yet [62,63]. The motivation for this study is to bridge the gap between MD and CFD to enable the simulation of microscopic droplet behavior in high-pressure fuel injection. The main objectives of this study are to identify the conditions at which the transition from subcritical to supercritical conditions occurs and develop new models for surface tension and evaporation rate of an *n*-dodecane droplet evaporating in a supercritical environment irrespective of the droplet size. The significance of this study lies in its potential to bridge the gap between MD and continuum modeling approaches for fuel droplets at supercritical which is of significant interest to the combustion community. The key findings from recent MD simulations, LGT, and continuum simulations at transcritical conditions are summarized below.

The first MD simulations of an oxygen droplet evaporating in a supercritical environment by Kaltz [64] provided scaling laws for droplets at the microscale using the Long-Micci method and investigated the validity of extrapolating MD results to macroscopic regimes by scaling the intermolecular potential parameters. More recently, Mo and Qiao [38] proposed a dimensionless timescale, referred to as liquid lifetime, as the governing timescale for the transition from sub- to supercritical conditions for a thin hydrocarbon layer evaporating into a supercritical nitrogen environment. Xiao [65] proposed a reduced pressure–temperature diagram showing the transcritical regime as a function of ambient temperature, pressure, and initial droplet size and showed that the time it takes for the droplet to fully transition, referred to as supercritical transition time depends on the initial droplet diameter. Gong [66,67] used the density distribution to distinguish the phase change process for a transcritical droplet and proposed a correlation to predict the transition from evaporation to single-phase GL diffusion for multicomponent fuels by introducing a critical dimensionless number based on the average displacement of fuel atoms. Wang [68] and Nguyen [69] considered an *n*-dodecane droplet evaporating in supercritical nitrogen and demonstrated the link between the onset of transition and the disappearance of surface tension. These studies proposed a classification for phase transition based on a supercritical transition time correlated with the disappearance of surface tension at the onset of single-phase diffusion [70,71]. However, recent studies have shown that the vanishment of the surface tension is not the main indicator of transition to GL diffusion [72]. The relationship between the decay of surface tension during transition to GL diffusion has not been understood, primarily

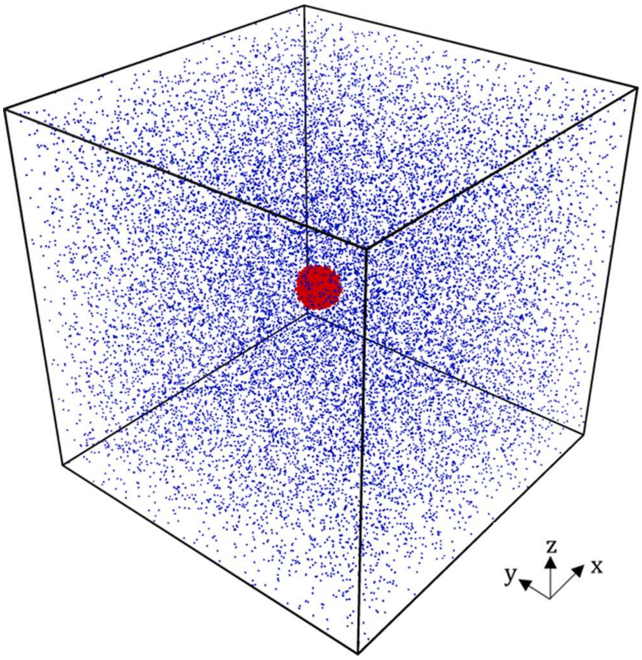

Fig. 2. Simulation set up illustrating a square box of size 65 nm and a 10 nm-diameter droplet. The blue color indicates nitrogen molecules, and the red color indicates *n*-dodecane molecules. The periodic boundary condition is applied in all directions.

because measuring the surface tension coefficient for multi-component mixtures approaching a critical state is very challenging experimentally and theoretically. LGT has been extensively employed to describe the transition from sub- to supercritical conditions. Dahms and Oefelein [26,39] compared the length scales using the Knudsen number (Kn); however, the selection of characteristic scale is ambiguous in the calculation of Kn and their approach is limited to the analysis of mean thermodynamic states. Kn is defined as the ratio of the mean free path of the gas molecules to a characteristic length scale of the flow, which indicates the transition from a rarefied regime ($Kn > 10$) to the continuum flow regime ($Kn < 0.01$). A new LGT theory for transcritical flows has been developed [19] to calculate fluid properties and surface tension coefficient. Thermodynamic potentials and governing equations have been modified for a binary system of heavy hydrocarbons and nitrogen using diffuse-interface theory. This model entails complex numerical modeling and approximations for gradient energy coefficients that limit its application to simple one-dimensional configurations. Several studies have attempted to shed light on the behavior of supercritical droplets using continuum flow simulations. Poplow [73] modeled the evaporation of a single supercritical droplet and showed that reaching the critical state is the primary indicator of transition to GL diffusion. A unified droplet vaporization model for use in simulations of high-pressure spray combustion was developed by Oefelein and Aggarwal [74,75] using a direct numerical simulation approach for *n*-hexane. Gilliard [76] coupled the diffuse-interface theory with the Navier-Stokes equations for hydrogen diffusion at transcritical conditions. Zhu [77] developed a model for *n*-heptane droplet vaporizing in a nitrogen environment to calculate the minimum pressure required for the transition from subcritical to supercritical. A continuum-based interface-resolving diffuse-interface method has been recently developed [69] to identify the underlying phase-exchange mechanisms consistent with MD findings. However, this study is limited to nanoscale droplets.

This study provides practical correlations for surface tension coefficient and evaporation rate during transcritical phase change to scale up MD simulations to the microscale. n-Dodecane is selected as the main fuel in this study as it has been commonly used as a surrogate fuel for diesel and kerosene in several experimental and computational studies at engine-relevant conditions [19,26,36,61,78,79]. A total of 210 simulations are conducted, maintaining the droplet temperature at a subcritical temperature of 363 K while varying the droplet diameter from 2 to 20 nm and nitrogen temperature varying from 300 K to 1100 K with 100 K intervals. The nitrogen pressure varies from 1 to 20 MPa to ensure the simulations capture a wide range of pressure and temperature from sub- to supercritical. The reduced temperature (T_r) ranges from 0.45 to 1.67 and reduced pressure (P_r) ranges from 0.56 to 11. The simulations are repeated for various droplet sizes to investigate the dependency of surface tension and evaporation behavior on droplet size and establish the relationship between phase change and surface tension and determine the conditions at which transition to GL diffusion occurs. Another novelty of this paper is the use of “undroplet time” as the transition timescale, which enables developing new models independent of droplet size to bridge the gap between MD and continuum simulations.

The paper is structured as follows. After introducing the computational methodology (Section 2), MD simulations are validated using (1) vapor–liquid equilibrium experiments in an n-dodecane-nitrogen binary system, (2) existing MD studies of an *n*-dodecane layer with a finite thickness evaporating in supercritical conditions, and (3) LGT predictions of surface tension coefficient and density across the interface (Section 3). Section 4 presents the simulation results and discussion. The correlation between the molecular behavior and undroplet time is described. The identified phase change behavior based on the undroplet time is compared with the phase change regime maps obtained using microscale experiments and nanoscale MD predictions. New surface tension coefficient and surface tension decay rate models are developed as a function of background temperature, pressure, and undroplet time independent of the droplet size. In addition, new evaporation rate models are created as a function of background temperature and undroplet time that capture the transition from subcritical evaporation to GL diffusion. The evaporation rate model is developed from three different approaches: (1) changes in the droplet size, (2) rate of droplet mass depletion, and (3) non-dimensional mass transfer number. The models developed in this study are readily accessible through the provided correlations in the paper and supplementary libraries submitted along the manuscript. Section 5 provides a summary of the research findings and conclusions.

2. Computational methodology

The transition of an *n*-dodecane droplet initially at subcritical temperatures with respect to its nominal critical point (658 K, 1.82 MPa) exposed to a supercritical nitrogen environment is studied. MD simulations are performed using an all-atom (AA) model where each atom is considered as a force site to provide a higher accuracy in predicting physical properties. The classical Newton’s equations are solved using the Verlet algorithm [80] using a large-scale atomic/molecular massively parallel simulator (LAMMPS) [81]. The interaction between *n*-dodecane and nitrogen molecules is modeled using the standard Lennard-Jones 6–9 potential, i.e., $\varnothing(r)$ following Eqn. (1).

$$\varnothing(r) = \epsilon\left(2\left(\frac{l}{r}\right)^9 - 3\left(\frac{l}{r}\right)^6\right), \tag{1}$$

Where ϵ is the depth of the potential well, l is the finite distance at which the inter-particle potential is zero, and r indicates the distance between the atoms. The Lennard-Jones potential consists of two terms: the van der Waals attraction term which models long-range dispersion forces, and the repulsion term, which describes the short-range steric interactions [82]. Although the Lennard-Jones potential offers a reasonably accurate representation of intermolecular forces, applying it to large molecules such as dodecane necessitates some considerations. The Lennard-Jones potential assumes molecular sphericity and non-

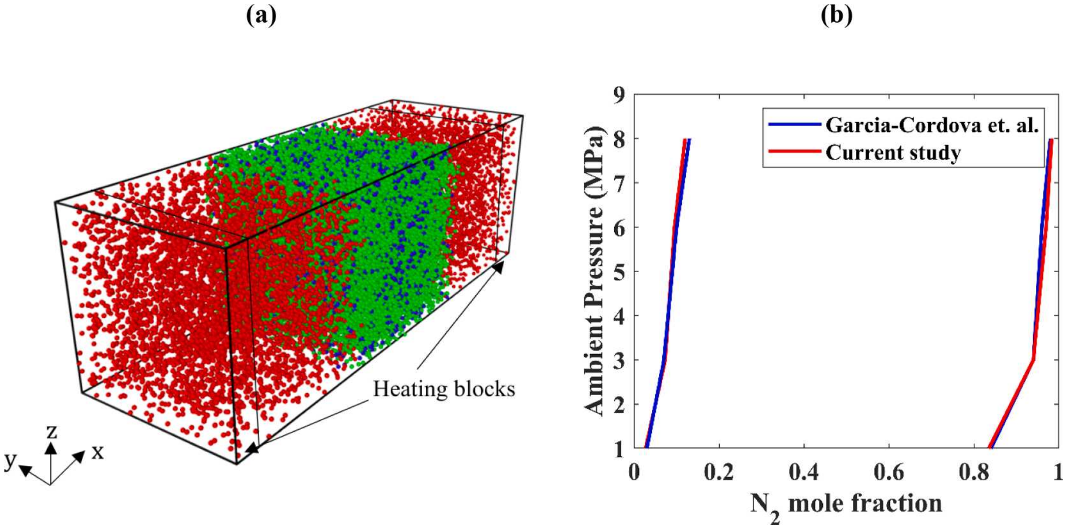

Fig. 3. (a) Initial setup of simulation box for the validation case: blue and green colors indicate CH$_3$— and CH$_2$—, respectively, and the red color indicates nitrogen molecules; (b) agreement of nitrogen mole fraction using MD for the binary n-dodecane-nitrogen vapor equilibrium [78].

directional interactions, which might not fully encapsulate the intricacies of larger, more complex molecules. For a large molecule like n-dodecane, these pairwise interactions can result in a considerable number of interaction terms, which can make simulations computationally expensive. To manage this deficiency, we have used two force fields, one for interatomic and one for intermolecular forces to ensure higher simulation accuracy. To predict the behavior of *n*-dodecane and nitrogen molecules, the class II Polymer Consistent Force Field (PCFF) is employed [83,84]. We develop the initial forcefield for interatomic forces using PCFF forcefield while the intermolecular forces are represented using Lennard-Jones potential interaction. In addition, Irving-Kirkwood [85] method is implemented to calculate the surface tension coefficient, i.e., σ for the Lennard-Jones binary fluid problem [65], which relates the surface tension to the fluctuations of the pressure tensor at the liquid–vapor interface. The simulation geometry is divided into N_s slabs of length L_z/N_s parallel to the X-Y plane (Fig. 2), where L_z is the total length of the computational domain to obtain the time-averaged pressure tensor components. The pressure tensor components are then used to compute the interfacial tension using the Irving-Kirkwood formula. The local normal and tangential components of pressure tensor, i.e., $p_N(k)$ and $p_T(k)$, respectively, are calculated in k's slab where $k = 1, \cdots, N_s$ following Eqns. (2)–(4):

$$\sigma = \frac{1}{2}\int_0^{L_z} (p_N(z) - p_T(z))dz, \tag{2}$$

$$p_N(k) = \langle n(k) \rangle k_B T - \frac{1}{V_{sl}} \left\langle \sum_{(i,j)}^{(k)} \frac{z_{ij}^2}{r_{ij}} \varnothing'(r_{ij}) \right\rangle, \tag{3}$$

$$p_T(k) = \langle n(k) \rangle k_B T - \frac{1}{V_{sl}} \left\langle \sum_{(i,j)}^{(k)} \frac{\frac{1}{2}\left(x_{ij}^2 + y_{ij}^2\right)}{r_{ij}} \varnothing'(r_{ij}) \right\rangle, \tag{4}$$

Where $n(k)$ is the particle density in slab k, $V_{sl} = L_x L_y L_z / N_s$ is the volume of the slab, x_{ij}, y_{ij}, z_{ij} and r_{ij} are the inter-particle distances, $\varnothing'$ is the derivative of the full inter-particle potential, and <> denotes the canonical ensemble average over all slabs.

2.1. Simulation setup

Ideally, our aim is to simulate micrometer-sized droplets, aligning with the dimensions of the fuel spray experiments detailed in the literature [36]. However, MD simulations in microscale are computationally very expensive and not currently feasible using all-atomic models considering the interactions between each atom. Therefore, 5–20 nm droplet sizes are considered in this study. A square box with a dimension of 65 nm is considered where a nanoscale (10 nm) *n*-dodecane droplet is placed at the center of the box, as shown in Fig. 2. The simulation box has a sufficiently large number of nitrogen molecules to ensure the pressure remains constant inside the box regardless of the ongoing evaporation. The number of molecules depends on the droplet size. For instance, a total of 770 *n*-dodecane and 18,000 nitrogen molecules are distributed randomly to represent a 10 nm droplet. The interface thickness is set by considering a 1 nm-thick shell around the droplet through which the equilibrium condition is achieved between the nitrogen and *n*-dodecane. During the equilibration phase of the simulation, the molecule velocity in this region are continuously adjusted to uphold the desired temperature. Furthermore, the liquid interacts with its own vapor, forming an interface with the ambient gas. The initial temperature of *n*-dodecane is set up to 363 K using the molecule velocity to represent the Engine Combustion Network (ECN) Spray-A conditions which represents a standard transcritical *n*-dodecane spray injected into supercritical nitrogen at 900 K and 6 MPa [86]. Nitrogen is initialized with a temperature of 900 K and pressure of 6 MPa, which acts as a heating source for the *n*-dodecane droplet. A layer of nitrogen molecules (1 nm thickness) at the edges of the simulation box acts as a thermostat to heat the entire domain. Nitrogen molecules are time-integrated using the NPT ensemble, which implies a constant number of atoms (N), constant pressure (P), and constant temperature (T). The simulations initially run for 100,000-time steps with a 2-fs time interval. Once the system is equilibrated, the micro-canonical ensemble, i.e., NVE, is applied for the primary time-integration simulation, where E and V imply constant energy and volume, respectively. The periodic boundary condition is applied in all directions. The NVE ensemble saves the data per 100-time steps, and the simulations run for another 1,000,000 time steps with 2 fs time intervals conducted using 4 nodes of 48 processors for 54 hours.

3. Validation simulations

In the following sub-sections, MD results are compared with (1) vapor–liquid equilibrium experiments in an *n*-dodecane-nitrogen binary system, (2) existing MD studies of an *n*-dodecane layer with a finite thickness evaporating in supercritical conditions, (3) LGT predictions of surface tension coefficient and density across the interface. For brevity, evaporation rate of an *n*-dodecane droplet in supercritical nitrogen

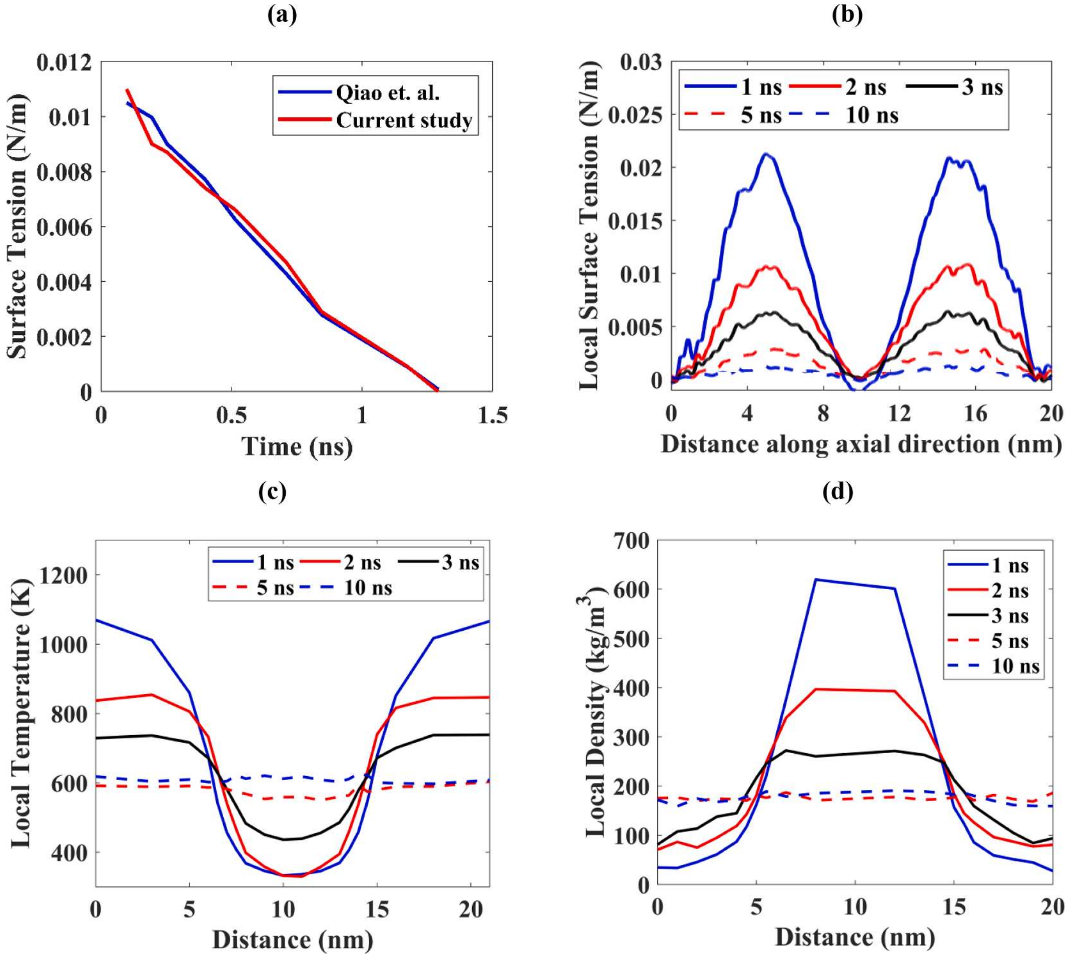

Fig. 4. (a) Surface tension varying with time for 1052 K ambient temperature and 20 MPa ambient pressure, compared with MD results of Mo and Qiao [38]; (b) local surface tension decay with time for 1052 K ambient temperature and 5 MPa ambient pressure; (c) local temperature, and (d) local density variation with time for 1052 K ambient temperature and 5 MPa pressure. The interface thickness is 2.5 nm.

compared with the previous MD studies has been discussed in Appendix I.

3.1. Vapor-Liquid equilibrium (VLE) in an n-dodecane-Nitrogen binary system

An *n*-dodecane-nitrogen binary system is simulated in a rectangular box (65 × 15 × 15 nm as shown in Fig. 3a) where the initial nitrogen and *n*-dodecane temperature is 500 K and 363 K, respectively. A united-atom approach is used for *n*-dodecane molecules by incorporating CH_3— and CH_2— as individual force sites. This approach differs from the all-atom approach, where the C- and H- in *n*-dodecane are considered separate force fields, as described in Section 2. The simulation is carried out for 1,000,000 steps with 2 fs time intervals. The center of the rectangular box is a 15 nm cube *n*-dodecane layer, and nitrogen molecules are distributed on either side of the *n*-dodecane layer. A heating block is applied at the ends of the rectangular box along the *x*-direction with a width of 5 nm on each side. A periodic boundary condition is applied in all directions, and an NVE ensemble is implemented [68]. The prediction of nitrogen mole fraction is in close agreement with the experiments conducted by Garcia-Cordova et al. [78], as shown in Fig. 3b.

3.2. Comparison of the surface tension coefficient with previous MD studies

A rectangular box (20 × 10 × 10 nm as shown in Fig. 3a) with an *n*-dodecane layer of 10 nm positioned at the center of the box is set at 363 K, and the background nitrogen is kept at 1052 K temperature, and 20 MPa pressure is considered consistent with Mo and Qiao's [38] MD study. The simulation is run with an initial interface thickness of 2 nm on either side of the *n*-dodecane block with a time step of 1 fs for 2,000,000 steps. To calculate the surface tension coefficient, the Irving-Kirkwood method [85] is employed. To this end, the derivative of the potential is calculated, followed by the canonical ensemble average of the density for each slab as outlined in Eqns. (2)–(4) [87]. The pressure values in the normal and tangential directions are extracted from the simulations, which are used for local surface tension calculation. The overall surface tension at a given time step is an integration of local surface tension over all the slabs, as stated in Eqn. (2). As shown in Fig. 4a, surface tension decay during the transition from subcritical to supercritical conditions closely agrees with MD simulations conducted by Mo and Qiao [38]. The local variation of surface tension, temperature, and density along the axial direction (see Fig. 3) are shown in Fig. 4b-d. This simulation is run at 5 MPa ambient pressure and 1052 K ambient temperature keeping all other parameters constant. As the simulation progresses, *n*-dodecane is heated by ambient nitrogen and transitions from a LL to a GL behavior. This transition is associated with an increase in *n*-dodecane temperature from 363 K to 600 K, as illustrated in Fig. 4c, and a decrease in the peaks of surface tension, as shown in Fig. 4b, followed by a decrease in local density, as evident in Fig. 4d. Due to the presence of two interfaces between nitrogen and *n*-dodecane, as this layer is positioned at the center of the box enclosed by nitrogen molecules, the surface tension plot exhibits two noticeable peaks along the axial direction (Fig. 4b). Consistently, temperature and density profiles exhibit two peaks on

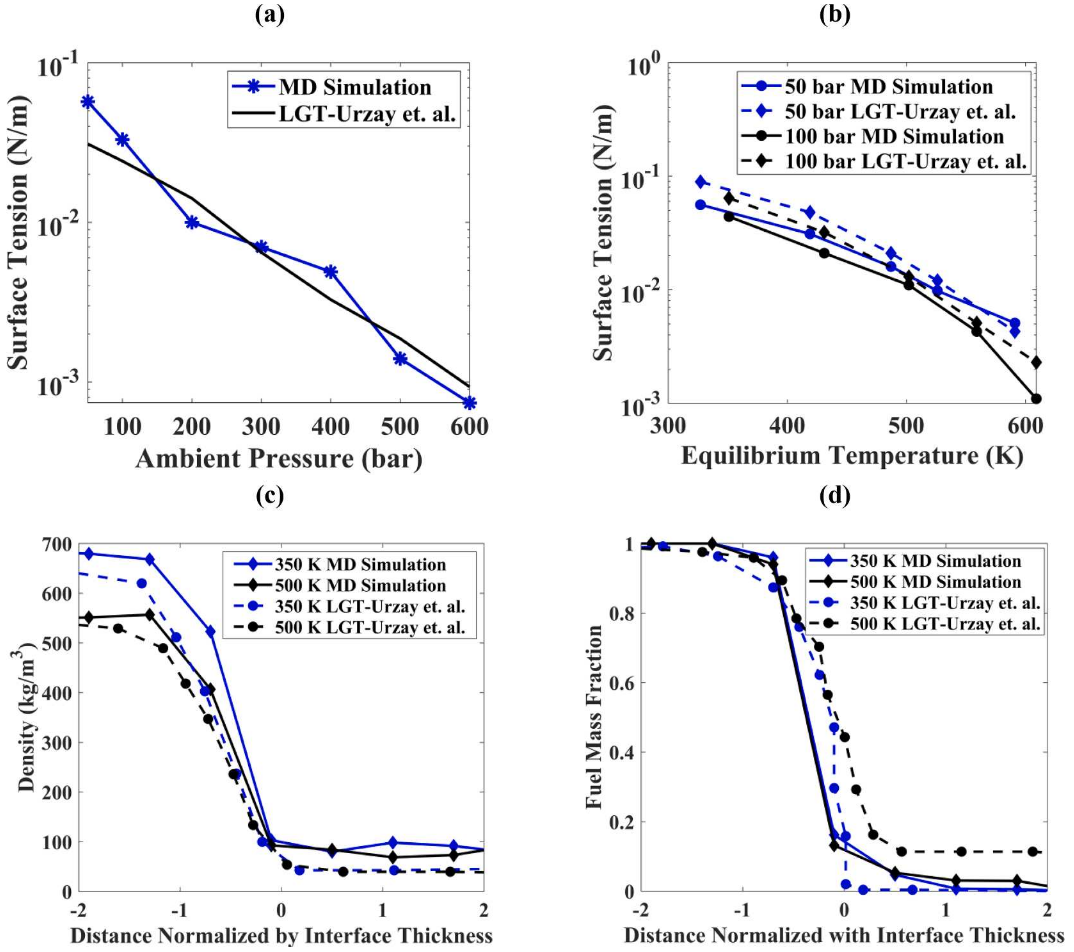

Fig. 5. Comparison between the current MD simulations and LGT [19] predictions: (a) surface tension variation with ambient pressure for a fixed equilibrium temperature of 450 K; (b) surface tension variation with change in equilibrium temperature for ambient pressure of 50 bar and 100 bar; (c) density and (d) n-dodecane mass fraction for 50 bar ambient pressure at 350 K and 500 K equilibrium temperature vs. distance across the interface normalized by the initial interface thickness.

either side of the bulk *n*-dodecane layer at the center of the computational domain, which is initially at 363 K. The interface thickness detected by the width of the two peaks on the surface tension profile initially increases with an increase in *n*-dodecane temperature and decreases in density until 3 ns, after which the interface disappears; the plots become a plateau and surface tension decays to zero.

3.3. Comparison with linear gradient theory predictions

MD results are compared with the recently-developed transcritical theory based on LGT proposed by Jofre and Urzay [19] for calculating the surface tension variation with ambient pressure and temperature. Equation (5) depicts the general form of surface tension coefficient σ using LGT, where κ is the gradient energy coefficient, $\hat{n}$ is the spatial coordinate normal to the interface, and $\frac{\partial \rho Y_f}{\partial \hat{n}}$ is the partial density gradient of the fuel in the normal direction. The fuel mass fraction is denoted by Y_f. The major shortcoming of this theory is its dependency on the gradient energy coefficients given by experiments which are not available for a wide range of conditions and require additional numerical interpolations. In addition, this theory assumes a mechanical and transport equilibrium at the interface and disregards viscosity, thermal conductivity, binary diffusion coefficient, and thermal diffusion ratio. For calculating the surface tension coefficient, the set of governing equations is solved and integrated with the state equation and the gradient-energy coefficient along with phase-equilibrium partial densities. As such, this theory entails a complex process, and the uncertainties in model constants limit the use of this theory in practical 2D and 3D CFD simulations.

$$\sigma = \int_{-\infty}^{\infty} \kappa \left(\frac{\partial \rho Y_f}{\partial \hat{n}}\right)^2 d\hat{n} \tag{5}$$

To compare MD and LGT predictions of surface tension coefficient, an isothermal *n*-dodecane-nitrogen system is considered with thermodynamic pressure ranging from 5 to 10 MPa and the equilibrium temperature varying from 350 to 500 K, which is lower than the critical temperature of the diffused mixture. A simulation box of size 20 × 5 × 5 nm is set up as shown in Fig. 3a at an equilibrium temperature of 450 K, and MD simulations are conducted to obtain the variation of surface tension coefficient. Fig. 5a shows the surface tension variation with background pressure varying from 5 to 60 MPa. A similar setup is used for surface tension variation with equilibrium temperature ranging from 350 K to 600 K at 50 bar and 100 bar, as shown in Fig. 5b compared with LGT predictions [19]. Fig. 5a–b shows that surface tension predictions based on MD simulations closely follow the LGT predictions. Surface tension coefficient decreases with an increase in pressure and temperature due to the transition from a two-phase behavior to a single-phase GL diffusion regime at transcritical conditions. The transcritical behavior persists even at increased pressure and temperature conditions as there is a co-existing region with equilibrium conditions at the interface. The variation of density and fuel mass fraction across the

Table 1
Range of parameters used for droplet MD simulations.

Parameter	Range
Initial droplet size, d_0 (nm)	2, 5, 10, 15, 20
Droplet initial temperature, T_0 (K)	363
Reduced background temperature ($T_r = \frac{T_b}{T_{critical}}$)	0.46–1.67 (with 7 intermediate states)
Reduced background pressure ($P_r = \frac{P_b}{P_{critical}}$)	0.56–11.1 (with 4 intermediate states)
Cubic simulation box size	65 times the droplet size
Boundary Conditions	Periodic in all directions.

interface normalized by the initial interface thickness between the current MD simulation and LGT [19] predictions for 5 MPa ambient pressure at 350 K and 500 K equilibrium temperatures are shown in Fig. 5c–d, respectively. These results indicate that MD simulations can replicate the same interfacial behavior as predicted by LGT within an average error of 9.4 %. Therefore, MD simulation results can provide a more efficient and more accurate means (i.e., no assumptions for interface) for calculating and implementing surface tension coefficient in CFD simulations at transcritical conditions.

4. Results & discussion

A total of 210 simulations are performed using the computational setup shown in Fig. 2, maintaining the droplet temperature at 363 K while varying the droplet diameter from 2 nm to 20 nm and nitrogen temperature varying from 300 K to 1100 K in 100 K intervals. The pressure varies from 1 to 20 MPa to represent a wide range of conditions from sub- to supercritical, representing T_r varying from 0.45 to 1.67 and P_r varying from 0.56 to 11.1, as outlined in Table 1. We firstly demonstrate the molecular behavior of an *n*-dodecane droplet and its correlation with the changes in surface tension and evaporation rate indicated with the change in the square of non-dimensional droplet diameter with time as well as the droplet depleted mass. Secondly, we introduce a non-dimensional time defined as the time the droplet disintegrates, and

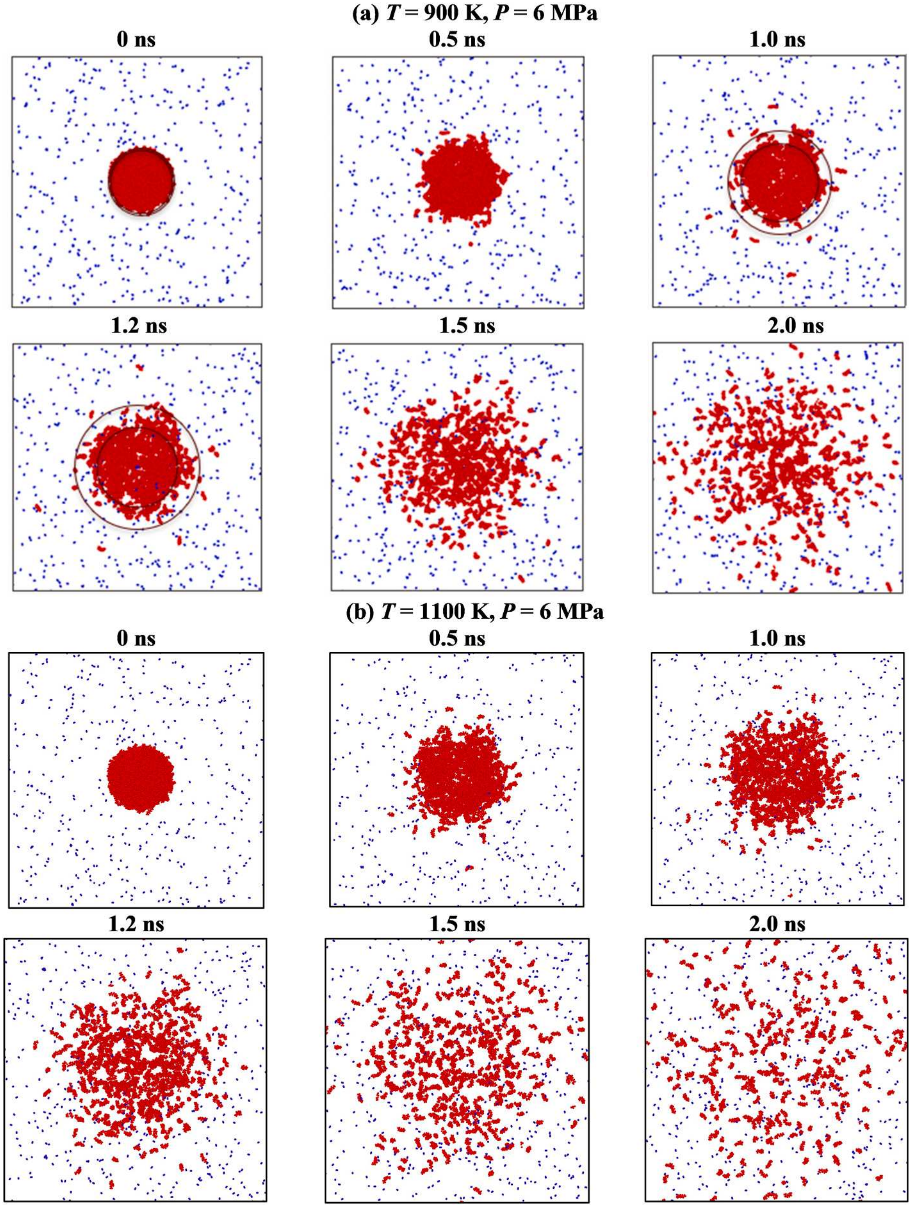

Fig. 6. The molecular behavior of a 10 nm *n*-dodecane droplet (red) exposed to nitrogen (blue) at (a) 6 MPa pressure and 900 K temperature. Concentric circles indicate interface thickening at t = 1 and 1.2 ns; (b) nitrogen at 6 MPa pressure and 1100 K temperature.

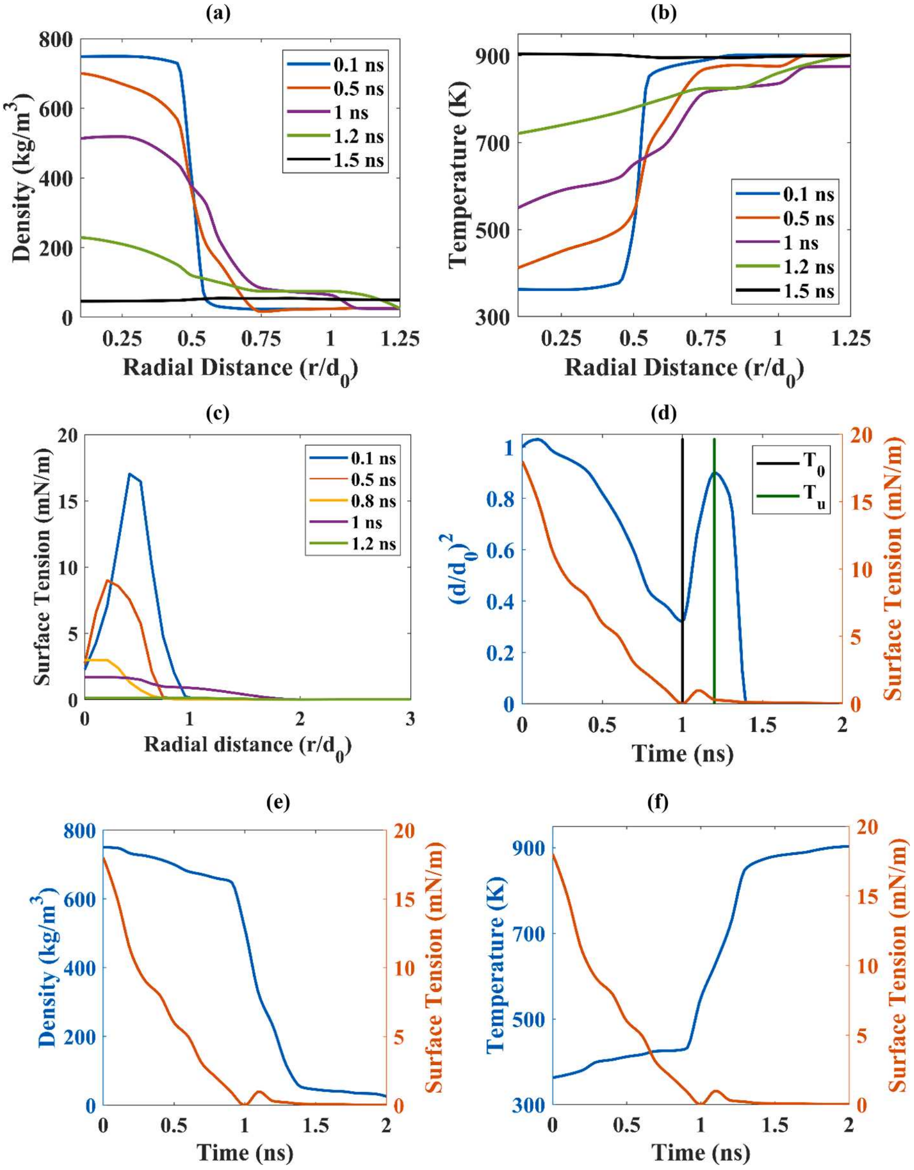

Fig. 7. Radial distribution of local (a) density, (b) temperature, (c) surface tension coefficient from the center of the droplet varying with time for 6 MPa pressure and 900 K temperature; (d) surface tension coefficient and evaporation rate variation with time: T_0 represents the time at which surface tension decays to zero and T_u indicates the undroplet time that occurs shortly after T_0; (e) surface tension coefficient and density at center of the droplet varying with time; (f) surface tension coefficient and temperature at center of the droplet varying with time.

nitrogen molecules penetrate the droplet core to represent new models for surface tension decay and evaporation rate independent of the droplet size. As will be shown, the undroplet time occurs after the time at which surface tension decays to zero.

4.1. Molecular behavior at transcritical conditions

The molecular behavior of a 10 nm-*n*-dodecane droplet at a subcritical temperature of 363 K exposed to supercritical nitrogen (6 MPa pressure, 900 K) consistent with the ECN Spray-A conditions [86] are chosen as the base case while new test cases are created by changing nitrogen temperature and pressure consistent with several recent MD studies as outlined in Table 1 [38,48,64–66,68,71]. In the sequential snapshots shown in Fig. 6, nitrogen and *n*-dodecane molecules are shown in red and blue, respectively. Two cases with a background temperature of 900 K in Fig. 6a and 1100 K in Fig. 6b are depicted. Fig. 7a-c shows the variation of density, temperature, and surface tension coefficient with time across the droplet/nitrogen interface starting from the droplet center (radial distance $r = 0$) for the same conditions as Fig. 6a.

Fig. 6a demonstrates that at 0.1 ns, the droplet exhibits a spherical shape and Fig. 7a-c indicate that the droplet density decreases as it is heated by the ambient nitrogen and the surface tension coefficient reaches its maximum value (i.e., 17.8 mN/m) close to the droplet interface. This behavior indicates that a very thin interface thickness initially exists between the *n*-dodecane droplet and nitrogen. At 0.5 ns, with an increase in droplet temperature, the surface tension coefficient is reduced during the evaporation phase, evident from the separation of *n*-dodecane molecules from the droplet core while the droplet core is still integrated (Fig. 6a). Although there is a drastic drop in surface tension at 1 ns (Fig. 7c), the molecular forces are still strong within the droplet core while evaporation occurs at a wider region within the interface indicated with two concentric black circles in Fig. 6a. This behavior is evident from the widening of the surface tension coefficient and reduction of droplet density with an increase in droplet temperature and transition from a LL to a GL fluid as it is heated by the surrounding

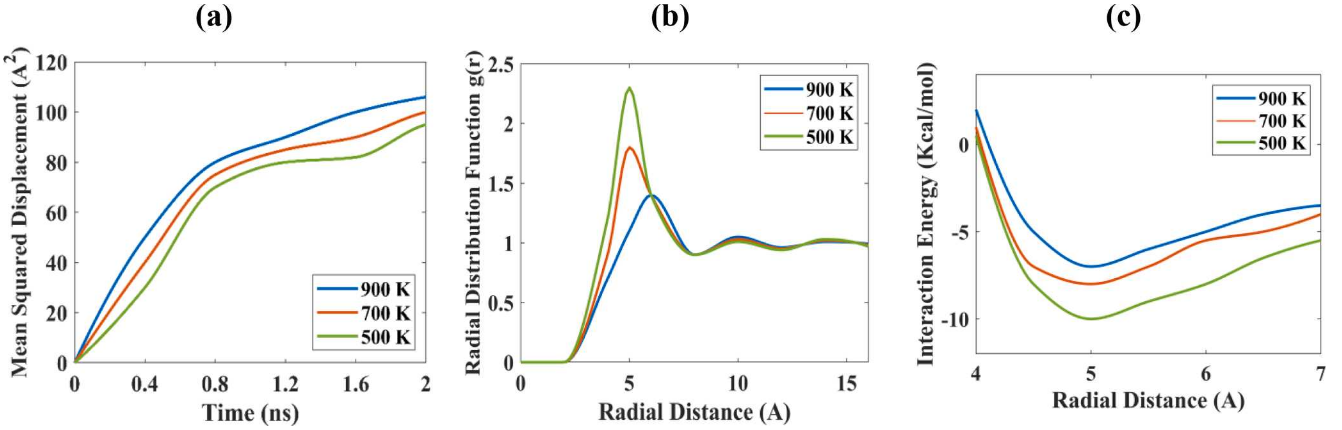

Fig. 8. (a) mean squared displacement; (b) radial distribution function, and (c) interaction energy for 6 MPa pressure and 10 nm droplet size varying nitrogen temperature (500, 700, and 900 K).

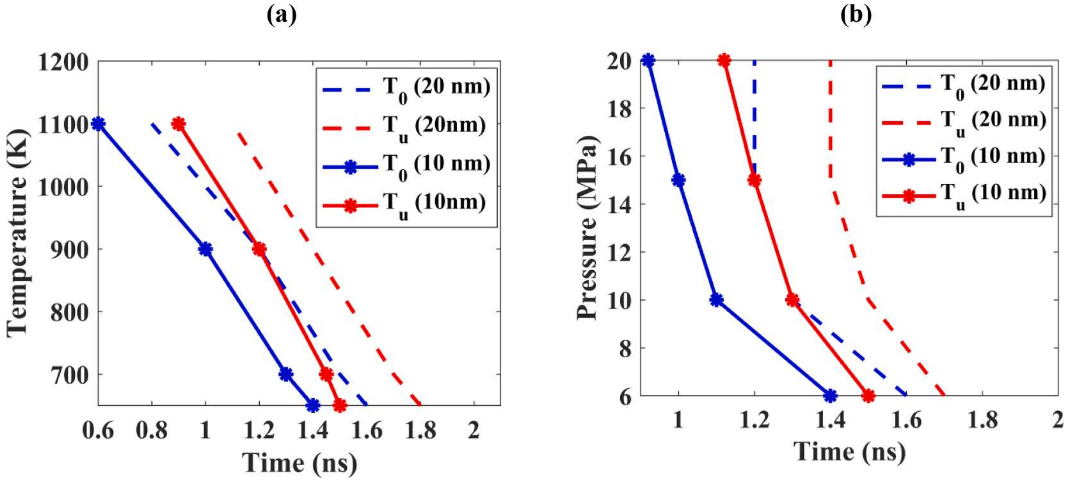

Fig. 9. Comparison of T_0 and T_u with time for selected droplet sizes: (a) temperature varies, keeping the pressure constant at 6 MPa; (b) pressure varies, keeping the temperature at 900 K.

nitrogen as shown in Fig. 7a-c. Such interface thickening behavior at transcritical conditions has been reported in several previous studies [19,36,38,47]. The droplet interface boundary is defined where the calculated density is equal to the average of the maximum and minimum density of the entire system, which is used as a reference point to calculate the instantaneous droplet diameter. The interface becomes thicker at 0.8 ns in Fig. 7a–c before it entirely diminishes at 1 ns, after which the droplet core disintegrates and n-dodecane and nitrogen mix under the GL diffusion regime as shown in Fig. 6a. Fig. 7c plots the local surface tension variation with the radial distance (r/d_0) from the center of the droplet at different simulation times. At $t = 0.1$ ns, the surface tension peaks and exhibit a sharp increase at $r/d_0 \sim 0.15$ which is the droplet interface. Whereas at $t = 1$ ns, the peak widens and makes a large plateau at $r/d_0 \sim 0.62$, corresponding to the interface thickening phase. The peak of the local surface tension starts flattening out as the interface thickness increases with time. In addition, the peak of the local surface tension starts moving towards the droplet center as the time progresses and surface tension decreases. This phase has been identified as "undroplet" phenomena in previous studies [38,68]. Fig. 6b shows that at a higher nitrogen temperature of 1100 K, the surface tension decays to zero at a faster rate between 0.5 ns and 2 ns which indicates a single-phase GL diffusion dominates during a major portion of the droplet's lifetime. To identify the transition from classical evaporation to GL diffusion, the changes in non-dimensional droplet diameter are plotted with time in Fig. 7d. Until 1 ns, the evaporation rate, i.e., $(d/d_0)^2$ where d_0 is the droplet initial diameter, decreases consistently with decay in surface tension. This observation is consistent with the conventional droplet evaporation theory governing subcritical conditions, which suggests that the square of the droplet diameter decreases linearly during this period [88,89]. As surface tension reaches zero at $t = T_0$, the evaporation rate spikes at a very high rate. The sudden expansion of the droplet size is due to the accelerated GL diffusion and penetration of nitrogen molecules into the droplet core in the absence of surface tension [68]. The evaporation rate reaches a peak at 1.2 ns in Fig. 7d representing the "undroplet" phenomenon denoted as T_u, where the droplet core is disintegrated, and the nitrogen molecules diffuse into the droplet core as shown in Fig. 6a at 1.5 and 2 ns. This behavior indicates that surface tension persists another ~1 ns before it decays to zero and the interface no longer holds the droplet together. Variation of density and temperature at the droplet center with time along with surface tension coefficient in Fig. 7e–f show that while the temperature at the droplet center is below the pseudo-boiling temperature of n-dodecane at 6 MPa (i.e., 651 K), the surface tension coefficient does not reach zero until 1 ns. These results show that surface tension endures until the entire core of the droplet becomes GL and exceeds the pseudo-boiling temperature. The observation is supported by the fact that it takes a longer time for the entire droplet core to reach the pseudo-boiling temperature. Droplet properties, e.g., temperature and density determine the difference between LL and GL. A LL fluid has a much higher density than a GL fluid. The transition occurs when the density of the droplet core decreases as

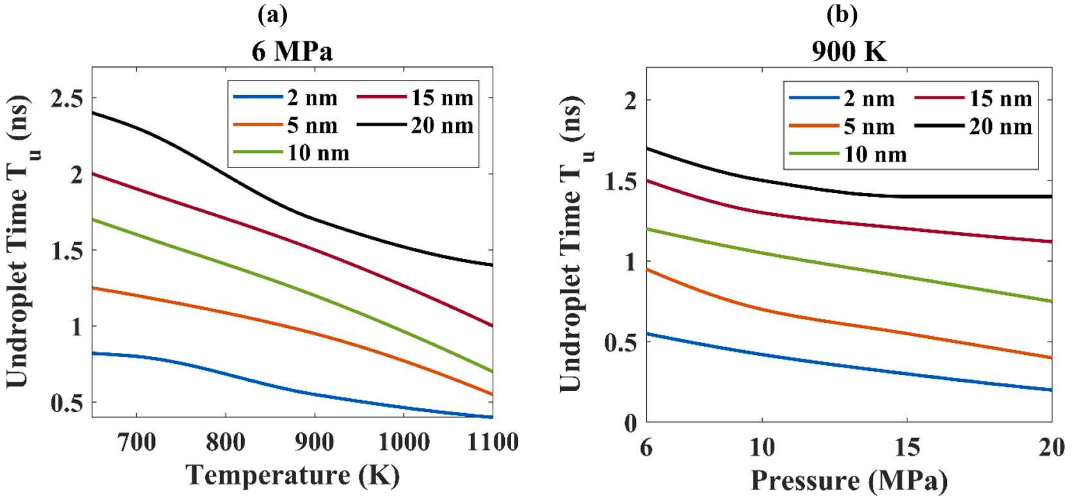

Fig. 10. Variation of T_u with time and droplet size: (a) temperature varies, maintaining the pressure constant at 6 MPa; (b) pressure varies, keeping the temperature constant at 900 K.

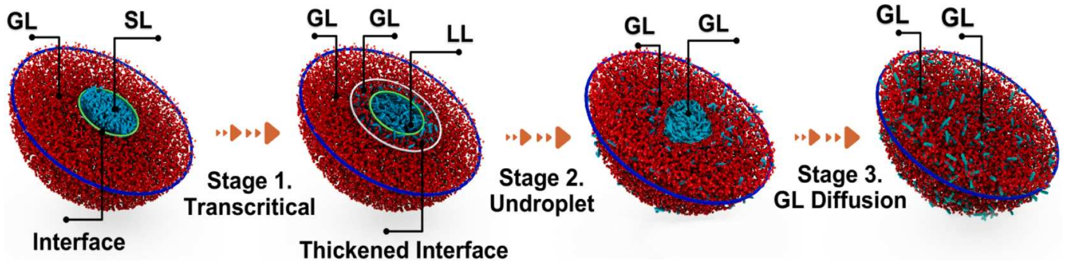

Fig. 11. A schematic of the phase change stages for a subcritical liquid (SL) droplet (cyan) in a gas-like fluid (GL) (red). Stage 1: interface turns into GL, thickens, and surface tension persists until the liquid core is GL; Stage 2: surface tension vanishes followed by undroplet; Stage 3: droplet becomes GL and diffuses into ambient (GL diffusion).

shown in Fig. 7e. The critical density of the droplet core, i.e., 226 kg/m^3 for *n*-dodecane at 650 K which is close to the nominal critical point of pure n-dodecane, is considered to determine crossing the Widom line and the transition from LL to GL fluid. The critical density is closely related to the Widom line as it is often identified as a region where the fluid properties change significantly. To further shed light on the relationship between surface tension and interfacial forces, mean squared displacement, which indicates the average displacement of *n*-dodecane molecules over time, has been calculated for a 10 nm-droplet evaporating in nitrogen with a temperature of 500, 700, and 900 K at 6 MPa. A higher mean squared displacement is observed in Fig. 8a with an increase in temperature. Calculation of radial distribution function (RDF) shows the probability density of finding a molecule at a certain distance from a reference particle in a system, further reflecting the interfacial interactions. The radial distribution shows a higher peak for 500 K at a shorter distance from the droplet center, indicating that the molecules are still holding higher potential energy resulting in higher surface tension. The peak of RDF drop shifts further away from the droplet center with an increase in temperature in Fig. 8b. This behavior demonstrates the interface thickening process shown in Fig. 6a. Calculation of interaction energy determines the potential energy associated with the pairwise interactions between molecules at the interface and quantifies the strength of the attractive and repulsive forces. The interaction energy decreases with an increase in temperature which indicates the droplet molecules are loosely correlated at the interface, which facilitates the transition to a GL diffusion regime, reduction of surface tension, and nitrogen penetration into the droplet core as shown in Fig. 8c. The details of the calculation of mean squared displacement, RDF, and interaction energy are given in Appendix II.

Fig. 9 shows the distinction between T_0 and T_u and their variation with pressure and temperature. The simulations have been repeated for two different droplet sizes, i.e., 10 and 20 nm diameter. Fig. 9a is an isobaric plot at 6 MPa, and Fig. 9b is an isothermal plot at 900 K showing the decrease in T_0 and T_u with an increase in nitrogen temperature and pressure, respectively. This figure shows that the transition from classical evaporation to GL diffusion, i.e., undroplet phenomena, is accelerated with an increase in background pressure and temperature. It is also evident that there is a lag between the time that surface tension decays to zero and the time that the undroplet phenomenon occurs, consistent with the molecular behavior shown in Fig. 6a. This behavior implies that even after reaching T_0, the transition to GL diffusion does not occur right after surface tension vanishment. This analysis shows that the transition from classical evaporation to GL diffusion is more accurately represented by T_u instead of T_0, which has been used as the critical time for transition to a supercritical phase in previous studies [38,66]. Fig. 10 shows T_u and T_0 increase with an increase in droplet size as a larger bulk volume needs to be heated to reach the GL phase.

Fig. 10a shows the variation of undroplet time (T_u) with droplet size for nitrogen temperature varying from 650 K to 1100 at a constant pressure of 6 MPa. This figure illustrates that undroplet time significantly increases with droplet size. This behavior further proves that the undroplet phenomenon occurs when the entire droplet core has reached a GL state. Fig. 10b shows that the undroplet time slightly decreases with an increase in pressure; however, its changes are more sensitive to the variation of background temperature.

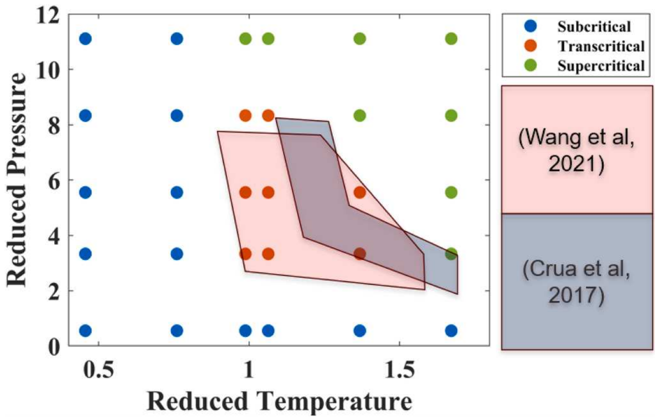

Fig. 12. A reduced pressure–temperature map showing subcritical (blue), transcritical (red), and supercritical (green) behavior detected using current MD simulations compared with the same regimes identified through experiments by Crua et al. [36] and simulations by Wang et al. [68].

4.2. Phase change regime map

Based on the analysis given in Section 4.1, three stages of phase transition are identified, which is consistent with the MD results presented by Wang et al. [68]. These three stages are schematically depicted in Fig. 11. The first stage, referred to as the transcritical phase, is characterized by a thickened interface while surface tension decays with time. The droplet core is mainly LL at this phase, while the interface temperature can exceed the pseudo-boiling temperature. The second stage is characterized by surface tension vanishment followed by the undroplet phenomenon when the entire droplet core becomes a GL fluid. Finally, GL diffusion occurs in the absence of surface tension.

Following the above phase change behavior, a phase change regime map for a droplet size of 10 nm with varying background pressure and temperature, keeping the *n*-dodecane temperature at 363 K, is depicted as a function of reduced temperature and reduced pressure in Fig. 12. The range of simulation parameters considered in this map is outlined in Table 1. Subcritical, transcritical, and supercritical behavior are denoted with blue, orange, and green symbols. Subcritical condition is identified in cases where the surface tension coefficient remained constant during the simulations. Transcritical behavior is characterized as the persistence of the surface tension coefficient for a finite time during the simulations, after which surface tension decays to zero.

This behavior occurs at P_r varying from 3.2 to 8.3 and T_r from 1.0 to 1.4. Finally, the supercritical regime is recognized in cases where the surface tension rapidly (less than 0.5 ns) decays to zero. This behavior is observed for $T_r > 1.5$ and P_r exceeding 8. The transcritical regime is compared with the criteria given based on Crua et al. experiments [36], which predicted P_r from 2 to 8 and T_r from 1.2 to 1.7 exhibited a transcritical behavior. This critical reduced pressure and temperature is slightly different than MD predictions, possibly due to challenges in optical diagnostics in capturing the accurate droplet morphology. However, the overall consistency with microscopic experiments indicates that the undroplet time can be used as the characteristic timescale to bridge between MD and experiments. A comparison of our results with the regime map based on MD simulation of *n*-dodecane droplets [68], demonstrates a good agreement in the prediction of the transcritical region. It is worth noting that despite differences in the molecular model setup between this study and [68], our utilization of the AA atom provides higher accuracy in predicting the interfacial forces. In the upcoming sub-sections, a comprehensive set of models will be presented. These models will provide a detailed analysis of undroplet time, surface tension coefficient, surface tension decay rate, and evaporation rate as a function of various parameters such as ambient pressure, temperature, and droplet size.

4.3. Surface tension model

In this sub-section, we present a quantitative analysis of the surface tension decay during the transition from subcritical to supercritical conditions. The decay in surface tension is a crucial input parameter to CFD solvers to incorporate the shift from a two-phase regime to a single-phase GL regime in practical liquid fuel injection applications. Fig. 13a–b show the variation of surface tension for two different droplet sizes keeping the initial temperature of *n*-dodecane constant at 363 K. For a constant background pressure of 6 MPa in Fig. 13a, surface tension initially drops but remains constant with time for a background temperature of 500 K which represents a subcritical temperature with respect to the nominal critical temperature of *n*-dodecane. This case represents a classical evaporation behavior throughout the simulations. The initial drop in surface tension is due to the temperature difference between the droplet and ambient nitrogen. For cases with temperature and pressure above the critical point of *n*-dodecane, i.e., 700 K and 900 K, we observe the transcritical phase schematically shown in Fig. 11, where the surface tension is decreasing but persists for a finite time for the 20 nm-droplet and decays to zero after 2 ns for the 10 nm-droplet. This behavior further confirms that it takes a longer time for a larger droplet to fully transition to a GL fluid, although the surface tension has

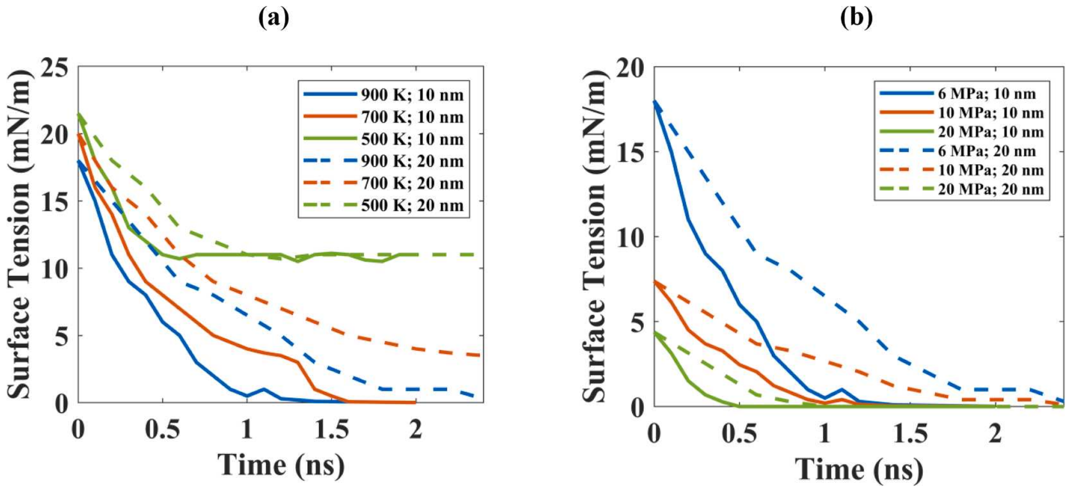

Fig. 13. Surface tension decay for a 10 and 20 nm-*n*-dodecane droplet exposed to nitrogen: (a) variable temperature at a constant 6 MPa pressure; (b) variable pressure at a constant 900 K temperature.

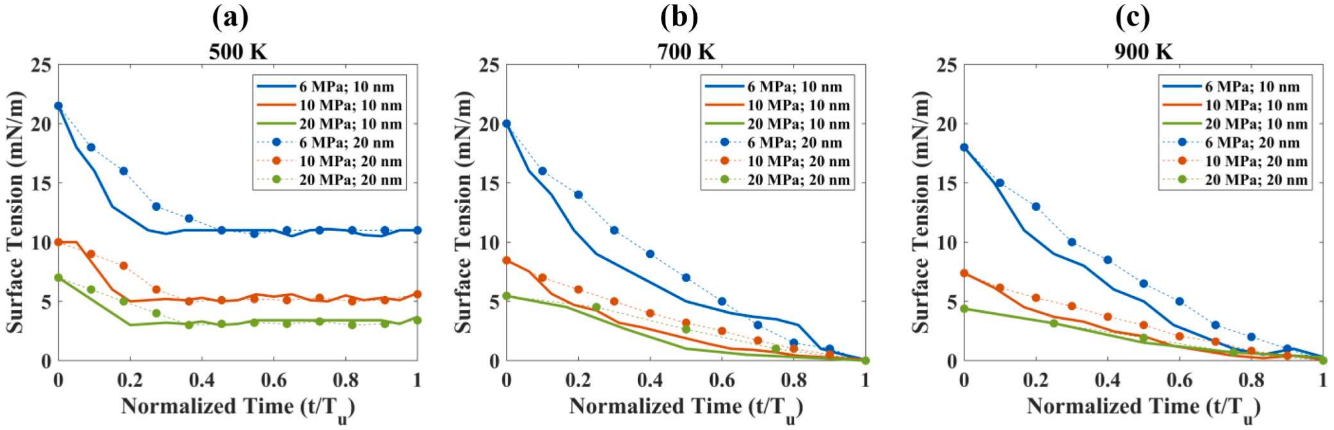

Fig. 14. Surface tension variation for a 10 and 20 nm-*n*-dodecane droplet exposed to nitrogen at variable temperature and pressure normalized with respect to the undroplet time T_u.

Table 2
Correlation coefficients for undroplet time (T_u), surface tension coefficient (σ), and the rate for the decay of surface tension ($\dot{\sigma}$).

Independent Variables	Correlation Coefficient for Dependent Variables		
	T_u	σ	$\dot{\sigma}$
Droplet diameter d_0(nm)	0.80	0.08	0.03
Background temperature T_b (K)	0.50	0.67	0.93
Background pressure p_b(MPa)	0.36	0.39	0.07
Normalized time t/T_u	–	0.74	–

reached zero. As was shown in Fig. 10, larger droplets need more time to entirely reach the GL state, after which the undroplet phenomenon prevails. It is also noted that surface tension decay occurs earlier at 900 K. Repeating the simulations for a constant background temperature of 900 K, varying the background pressure from 6 to 10 and 20 MPa in Fig. 13b shows that surface tension decays faster at higher pressures and is delayed for larger droplets at all pressures.

In Fig. 14a–c, surface tension coefficient is shown as a function of a non-dimensional time normalized with respect to the undroplet time (T_u), which is a more accurate threshold for transition to GL diffusion as discussed earlier. For each case, the normalized time, i.e., t/T_u has been calculated based on separate simulations which differ in the background pressure, temperature, and droplet size as presented in Fig. 10. Fig. 14a shows that at a subcritical temperature of 500 K, surface tension does not depend on the droplet size while it decreases with an increase in pressure. With further increases in background temperature to 700 K (Fig. 14b) and 900 K (Fig. 14c), the dependency of the surface tension to droplet size further increases. A noticeable disparity in surface tension coefficient value is observed between the subcritical temperature (500 K) and a temperature in close proximity to the critical temperature of *n*-dodecane (i.e., 700 K), with a relatively insignificant change observed with further temperature escalation (900 K). By increasing the pressure to 10 and 20 MPa, the difference in surface tension diminishes. This behavior indicates that the background temperature has a more profound effect on surface tension than the pressure at transcritical conditions. Additionally, the surface tension coefficient demonstrates a minor variation of about 3.1% between droplet sizes, maintaining nearly constant values at a constant temperature. Therefore, a new model for surface tension coefficient as a function of undroplet time is developed based on the MD results. For this purpose, two different methods, namely multiple regression, and gradient-boosted tree model have been used. It is noted that, unlike the multiple-regression model, the gradient boosted tree does not offer a straightforward relationship between the independent and response variables. However, the gradient-boosted tree model more accurately predicts the nonlinear relationship between the undroplet time and independent variables as it is not constrained by the linearity assumption [90,91]. Moreover, the gradient-boosted tree is a powerful ensemble-based model that allows for achieving higher accuracies by combining multiple algorithms to improve otherwise weak models [91]. The generated data from the gradient boosting model has been meticulously organized and is available as Appendix B supplementary material accompanying this paper. As a starting point, a correlation matrix is created based on Pearson's product-moment correlation on the entire dataset (Table 1) [92,93] to find the pairwise correlation of independent variables, namely pressure, temperature, and droplet size where a higher correlation coefficient indicates stronger dependence. The correlation matrix helps in identifying the variables that have the most impact on the dependent variable and are most likely to affect the outcome of the model. Table 2 represents the correlation coefficient for T_u. The pairwise correlation is the highest for droplet diameter and temperature, while pressure is weakly correlated with T_u. The correlation matrix for the surface tension coefficient (σ) shown in Table 2 indicates a strong correlation between surface tension, undroplet time, and temperature and a weaker correlation with droplet size and pressure. This analysis corroborates the previous assertion that undroplet time is the key characteristic timescale in transcritical behavior which is dependent on the droplet size.

A model for undroplet time T_u (ns) as a function of background temperature $T_b(K)$, pressure $p_b(MPa)$ and droplet diameter d_0 (nm) is developed (Eqn. (6) using the multiple regression model. This equation can be used in conjunction with the surface tension model given in Eqn. (7), which predicts surface tension σ (N/m) as a function of background temperature $T_b(K)$, pressure $p_b(MPa)$, droplet diameter d_0 (nm), and normalized time t/T_u. For training the multiple-regression and gradient-boosting ML algorithms utilized in this study, 75 % of the total simulation data points are used and 25 % of the total empirical data points are employed as test cases. The R^2 coefficient of determination is used to assess the accuracy of each model. It measures the proportion of variance in the dependent variable represented by the independent variables in the regression model. A higher R^2 value indicates a better fit of the model to the data, with values closer to 1 indicating a stronger relationship between the variables. For T_u, R^2 is 0.97 and 0.99, while for σ, R^2 reduces to 0.72 and 0.97 for the multiple regression and gradient-boosting methodologies, respectively. The agreement between the training data set and testing set for both methods and for T_u and σ are depicted in Fig. 15.

$$T_u(ns) = \left(-3.15 \times 10^{-2}\right)p_b(MPa) + \left(-1.74 \times 10^{-3}\right)T_b(K) + \left(6.69 \times 10^{-2}\right)d_0(nm) + 2.25, \quad (6)$$

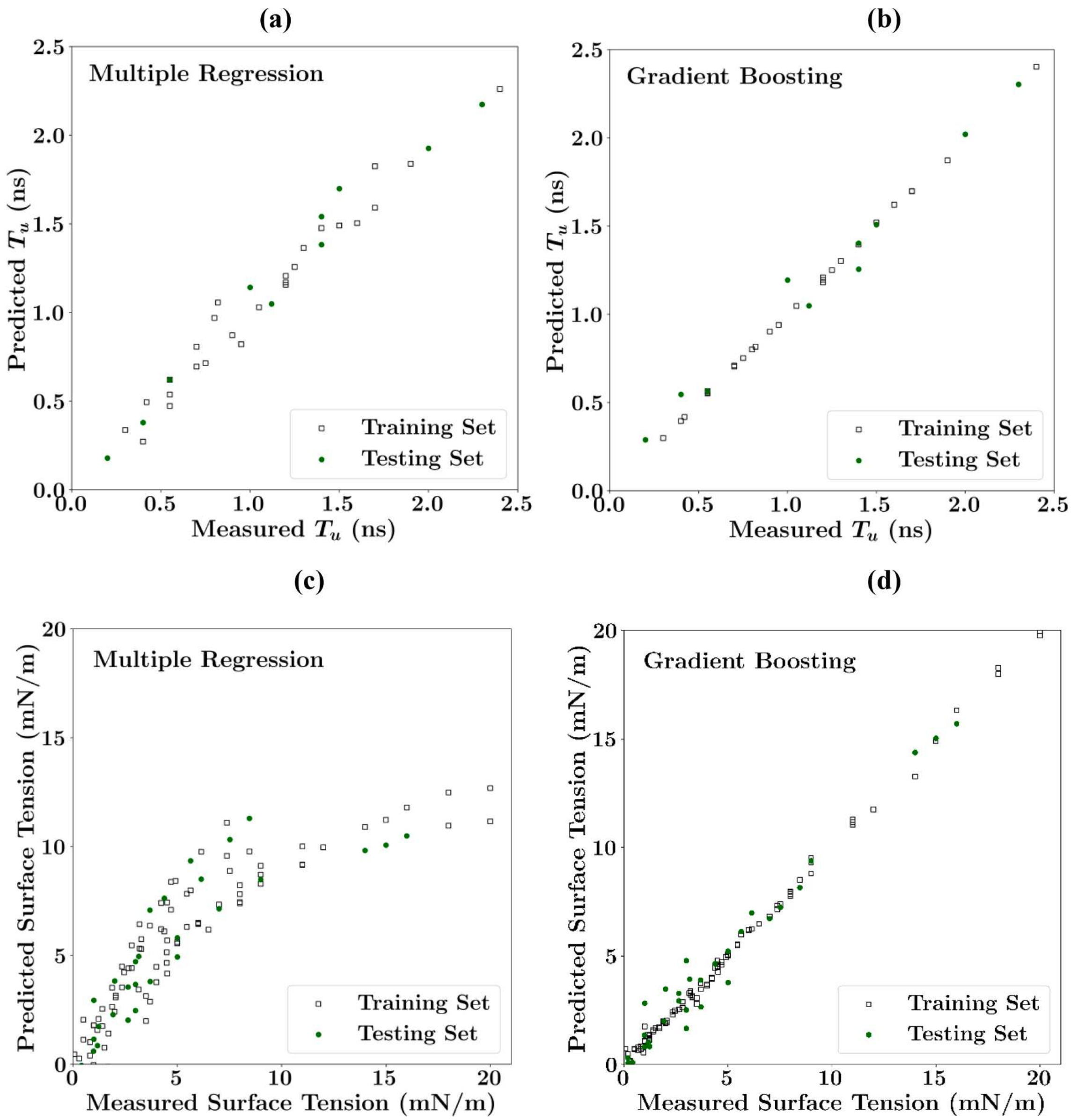

Fig. 15. Predicted undroplet time T_u *vs.* simulation using (a) multiple regression and (b) gradient boosted tree methods. Predicted surface tension σ *vs.* simulation using (c) multiple-regression, and (d) gradient-boosted tree methods.

$$\sigma(N/m) = (-3.47\times10^{-4})p_b(MPa) + (-9.99\times10^{-7})T_b(K) + (1.52\times10^{-4})d_0(nm) + (-1.07\times10^{-2})(t/T_u) + (1.24\times10^{-2}) \quad (7)$$

$$\dot{\sigma}(N/ms) = (2.87\times10^{2})T_b{}^2(K) - (1.28\times10^{5})T_b(K) + (1.1\times10^{4})p_b(MPa) - (5.9\times10^{3})d_0(nm) \quad (8)$$

$$\dot{\sigma}(N/ms) = (2.87\times10^{2})T_b{}^2(K) - (1.28\times10^{5})T_b(K) \quad (9)$$

Another parameter of crucial importance to establish continuum models for transcritical droplets is the rate of decay of surface tension during droplet transition from subcritical to supercritical conditions. Experimental analysis of microscopic droplets at transcritical conditions has revealed that the transition from evaporation to GL diffusion, which occurs over a finite duration is related to the decay of surface tension to zero [35]. Therefore, it is crucial to determine the rate of surface tension decay to gain insights into the transcritical behavior in microscale. To this end, the rate of decay of time-averaged surface tension is calculated for 5, 10, and 20 nm droplets, varying the background temperature and pressure. Fig. 16a shows that the background pressure exhibits a minor effect while temperature plays a more pronounced effect on the surface tension decay rate, as shown in Fig. 16b. The decay rate is higher as the temperature increases and varies linearly until reaching 6 MPa after which the surface tension decay rate reaches a plateau for higher pressures. Interestingly, the rate of decay of surface tension does not depend on the droplet size. The correlation coefficients for $\dot{\sigma}$ outlined in Table 2 confirms that the correlation is stronger for background temperature, and the droplet size is weakly correlated with $\dot{\sigma}$. This finding holds great promise for bridging the existing divide between nanoscale and microscale simulations of transcritical droplets. To this end, a new regression model is developed for $\dot{\sigma}$ (N/ms) as a function of background temperature $T_b(K)$, pressure $p_b(MPa)$ and droplet diameter d_0 (nm) as outlined in Eqn. (8) with an R^2 coefficient equal to 0.99. A simplified version of the surface tension decay rate model as a function of background temperature is developed by neglecting the droplet size and background pressure that exhibited a much weaker correlation with the surface tension decay rate, as depicted in Table 2. This model is outlined in Eqn. (9) and shown in Fig. 16a. The average R^2 value in the simplified version of the

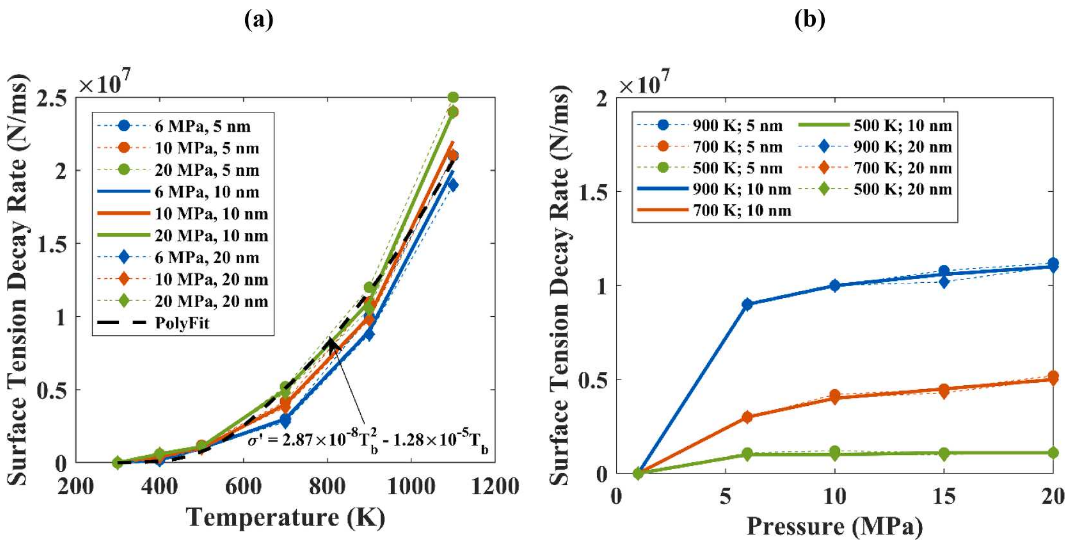

Fig. 16. (a) Time-averaged surface tension decay rate varying with temperature for 6, 10, 20 MPa pressure and 5, 10, 20 nm droplet size; (b) time-averaged surface tension decay rate variation with pressure for 500, 700, 900 K temperature and 5, 10, 20 nm droplet size.

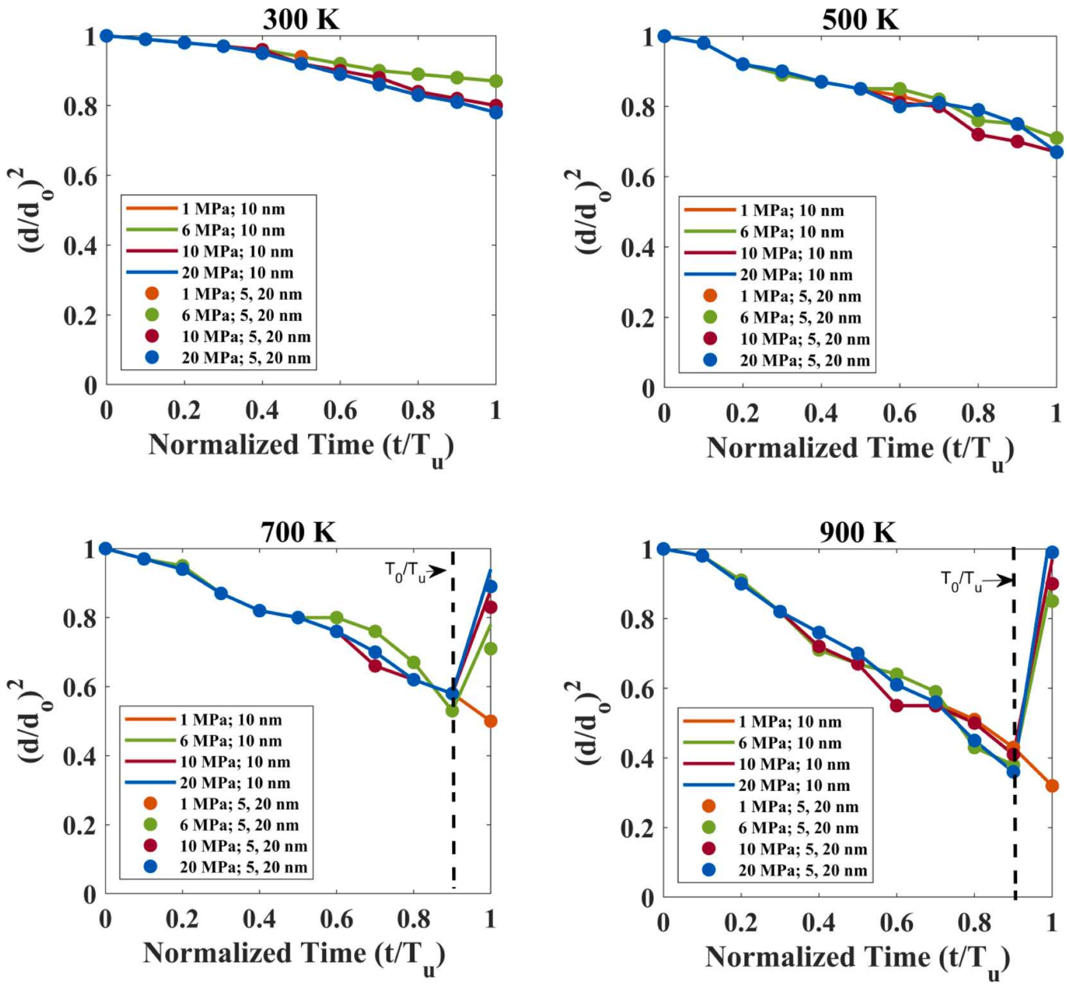

Fig. 17. Evaporation rate varying with pressure, temperature, and droplet size *vs.* normalized time with respect to the undroplet time, i.e., t/T_u.

surface tension decay rate model over the entire dataset is 0.99, which shows that neglecting pressure and droplet diameter in the surface tension decay rate is justified. These surface tension models can be used as an input to CFD solvers.

4.4. *Evaporation rate model*

The evaporation rate is first calculated by representing the non-dimensional droplet diameter varying with time, normalized with

Table 3

Correlation coefficients for evaporation rate $(d/d_0)^2$.

Independent Variables	Correlation Coefficient
Droplet diameter d_0(nm)	0.00
Background temperature T_b (K)	0.34
Background pressure p_b(MPa)	0.04
Normalized time t/T_u (-)	0.87

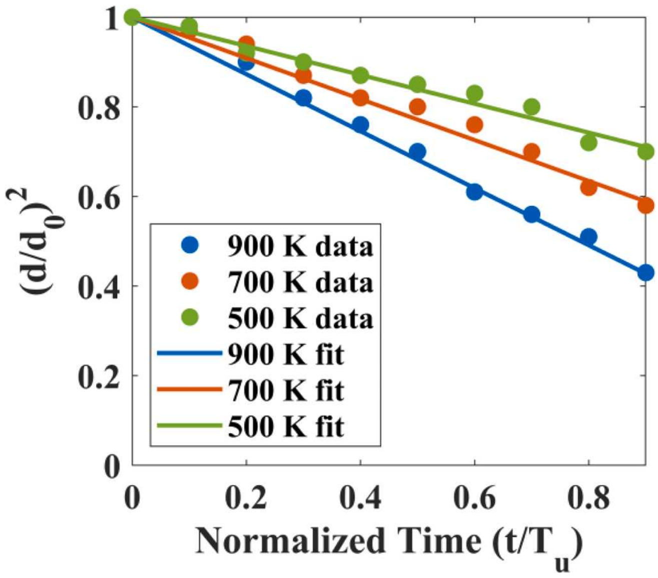

Fig. 18. Agreement of the linear evaporation rate model with non-dimensional droplet data varying with non-dimensional time normalized with respect to undroplet time T_u, varying the temperature.

respect to the undroplet time, i.e., t/T_u in a similar approach as the surface tension coefficient discussed in Fig. 14a. T_u follows the trend shown in Fig. 10. Fig. 17a-d show the variation of $(d/d_0)^2$ for 5, 10, and 20 nm *n*-dodecane droplets initially at 363 K exposed to nitrogen at four different background temperatures (300, 500, 700, and 900 K) and pressures (1, 6, 10, and 20 MPa) which span from sub- to supercritical conditions. These figures show that the evaporation rate is mainly dictated by the background temperature, even at supercritical pressures (6, 10, and 20 MPa), and increases with an increase in temperature. At subcritical temperatures (300 and 500 K), the evaporation rate remains linear throughout the simulations, representing a classical evaporation behavior. Beyond the critical temperature (700 and 900 K), the evaporation rate initially follows a linear trend. However, upon reaching the point of zero surface tension, indicated by the vertical line $\frac{T_0}{T_u}$, there is a sudden and significant increase in the evaporation rate. The significant expansion of the droplet is associated with the undroplet phenomenon and droplet core disintegration coincided with penetration of nitrogen molecules into the droplet core, as was shown in Fig. 6a at 1.5 ns. Fig. 17 shows that by neglecting the fluctuating nature of MD results, the evaporation rate is not dependent on the pressure. These results indicate that $\frac{T_0}{T_u}$ 0.9, is the common timescale between all cases irrespective of the droplet size that represents the transition from a subcritical two-phase regime to a supercritical single-phase GL diffusion regime. In the previous section, Pearson's correlation matrix was introduced to determine the strength of pairwise correlations. Applying this method to the evaporation rate (Table 3) confirms that the droplet diameter and pressure exhibit a weak correlation with the evaporation rate.

The multiple regression and gradient-boosting model, where 75 % of the total simulation data points are used, and 25 % of the total empirical data points are applied as test cases. A new evaporation rate model as a function of background temperature is developed for the entire dataset (Table 1) as outlined in Eqn. (10) to predict the evaporation rate $(d/d_0)^2$ as a function of background temperature $T_b(K)$, pressure $p_b(MPa)$, and normalized time t/T_u. The R^2 coefficient of determination is 0.87 and 0.99 for the multiple-regression and gradient-boosting methodologies, respectively. The agreement between the training set and the testing sets for the evaporation rate is depicted in Appendix III.

The correlation matrix outlined in Table 3 shows that the evaporation rate is weakly dependent on droplet size and pressure. This finding motivates generating a simplified model for evaporation rate by neglecting pressure and considering the non-dimensional time and background temperature in Eqn. (11), where the undroplet time is given in Eqn. (6). Fig. 18 shows that Eqn. (11) is in close agreement with the simulations for three selected conditions (i.e., 500, 700, and 900 K, 6 MPa pressure, and 10 nm droplet diameter). An interesting observation made in the study is that for a constant temperature, the non-dimensional droplet diameter relative to the initial droplet size varies linearly with the non-dimensional time normalized with respect to the undroplet time. The R^2 value for this linear model is $\sim$ 0.99 for each cases shown in Fig. 18. These results indicate a regular and predictable behavior of droplet evaporation at transcritical conditions, which could be significantly useful for scaling up MD simulations to microscale.

$$(d/d_0)^2 = \left(-1.11\times10^{-3}\right)p_b(MPa) + \left(-3.88\times10^{-4}\right)T_b(K) + \left(-5.18\times10^{-1}\right)(t/T_u) + 1.33, \tag{10}$$

$$(d/d_0)^2 = \left(-3.88\times10^{-4}\right)T_b(K) + \left(-5.18\times10^{-1}\right)(t/T_u) + 1.33 \tag{11}$$

4.5. *Mass depletion rate*

In this sub-section, the droplet mass depletion rate is calculated for the same cases presented in Table 1. Both mass depletion and droplet size reduction provide complementary information about the evaporation process. Mass depletion is defined based on the rate at which the mass of the liquid droplet decreases over time during droplet transition from sub- to supercritical conditions and is directly related to the evaporative flux. Mass depletion accounts for the interfacial mass transfer. The mass depletion is normalized with respect to the droplet's initial mass (M_0). The time is normalized with respect to the undroplet time, i.e., t/T_u consistent with the droplet evaporation rate discussed in Section 4.4. Fig. 19 shows the variation of the normalized mass depletion (M/M_0) for 5, 10, and 20 nm *n*-dodecane droplets initially at 363 K exposed to nitrogen at four different background temperatures (300, 500, 700, and 900 K) and pressures (1, 6, 10, and 20 MPa), similar to the evaporation rate depicted in Fig. 17. Fig. 19 shows that the normalized mass depletion increases monotonically for the subcritical temperature of 300 K regardless of pressure and similarly for the subcritical case of 1 MPa pressure. At transcritical temperatures, specifically at 700 and 900 K, the mass depletion during evaporation becomes increasingly prominent as time progresses. During the classical evaporation behavior at 700 K, i.e., $t/T_u = 0.8$, the droplet only loses 20 % of its mass, while during the GL diffusion phase, the droplet mass loss increases by a factor of four past the undroplet time. The attainment of a mass depletion value of one signifies that the droplet has undergone complete diffusion, with all its components dispersed throughout the nitrogen surrounding. Another interesting evaporation behavior occurs for 700 K, which is closer to the nominal critical temperature of *n*-dodecane for t/T_u varying from 0.8 to 1.2. The rate of mass depletion increases by a factor of 2.5 during this period which overlaps with the interface thickening behavior and the transcritical phase where surface tension effects persist and prevents the nitrogen molecules from penetrating the droplet core, as shown in Fig. 6a. At this phase, the evaporation mainly occurs within the thickened interface as schematically shown in Fig. 11. The interface thickening period is shorter for the 900 K case as transition to GL

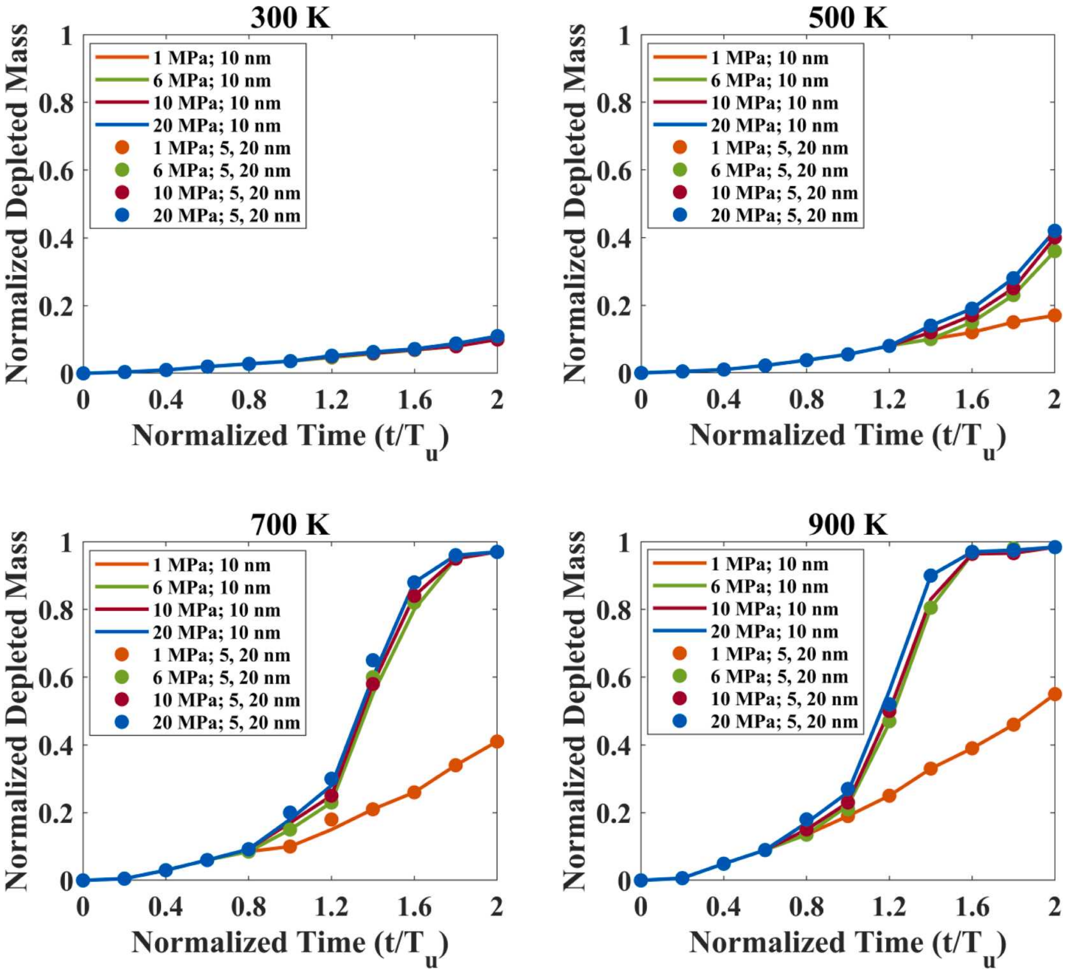

Fig. 19. Normalized mass depletion varies with pressure, temperature, and droplet size *vs.* normalized time with respect to the undroplet time, i.e., t/T_u.

Table 4
Correlation coefficients for normalized mass depletion (M/M_0).

Independent Variables	Correlation Coefficient
Droplet diameter d_0(nm)	0.00
Background temperature T_b (K)	0.36
Background pressure p_b(MPa)	0.14
Normalized time t/T_u (-)	0.72

behavior is accelerated with an increase in background temperature. This behavior indicates that the transcritical phase is identified with an increased mass depletion rate in the presence of surface tension before the undroplet phenomenon occurs.

As depicted in Fig. 19, there is a significant increase in mass depletion close to the undroplet time for 700 and 900 K cases at $t/T_u = 1$. The substantial increase in mass depletion over time at transcritical temperatures is a consequence of the strong coupling between thermal and species diffusion. The elevated temperatures intensify the GL diffusion rates, leading to a more rapid depletion of droplet mass. The droplet core disintegration occurs henceforward, and a finite time is necessary to complete this transition. This shift in evaporation behavior is consistent with the sharp increase in the droplet size past the undroplet time, as indicated in Fig. 17. The changes in mass depletion are more pronounced with an increase in temperature; however, even at a subcritical temperature of 500 K, mass depletion increases with an increase in pressure past the critical point (i.e., 6, 10, and 20 MPa), as shown in Fig. 19. Interestingly, the increase in mass depletion is not highly affected by an increase in pressure at transcritical temperatures of 700 and 900 K, and the mass depletion monotonically increases at a lower rate for a subcritical pressure of 1 MPa. This intriguing behavior suggests that the rate of evaporation is primarily influenced by temperature beyond the critical points, while the effects of droplet size and pressure become less significant in determining mass depletion. However, at subcritical temperatures, the role of pressure becomes more prominent in shifting the evaporation behavior. The calculated pairwise correlations for mass depletion shown in Table 4 corroborate that temperature is strongly correlated with mass depletion, and pressure is less influential.

A new normalized mass depletion model as a function of background temperature, pressure, and undroplet time is developed for the entire dataset (Table 1) as outlined in Eqn. (12) to predict the normalized mass depletion (M/M_0) as a function of background temperature $T_b(K)$, pressure $p_b(MPa)$, and normalized time t/T_u. It is noted that T_u is calculated using Eqn. (6). This model accounts for a wide range of conditions, from sub- to supercritical conditions. The R^2 coefficient of determination is 0.69 and 0.97 for the multiple regression and gradient-boosting methodologies, respectively. The agreement between the training set and the testing sets for the depleted mass is depicted in Appendix III. The developed mass depletion rate model can serve as a valuable input for adjusting the mass transfer coefficient in classical evaporation models that do not consider the transcritical effects.

$$(M/M_0) = \left(5.98 \times 10^{-3}\right)p_b(MPa) + \left(7.66 \times 10^{-4}\right)T_b(K) + \left(3.74 \times 10^{-1}\right)(t/T_u) - 0.663 \quad (12)$$

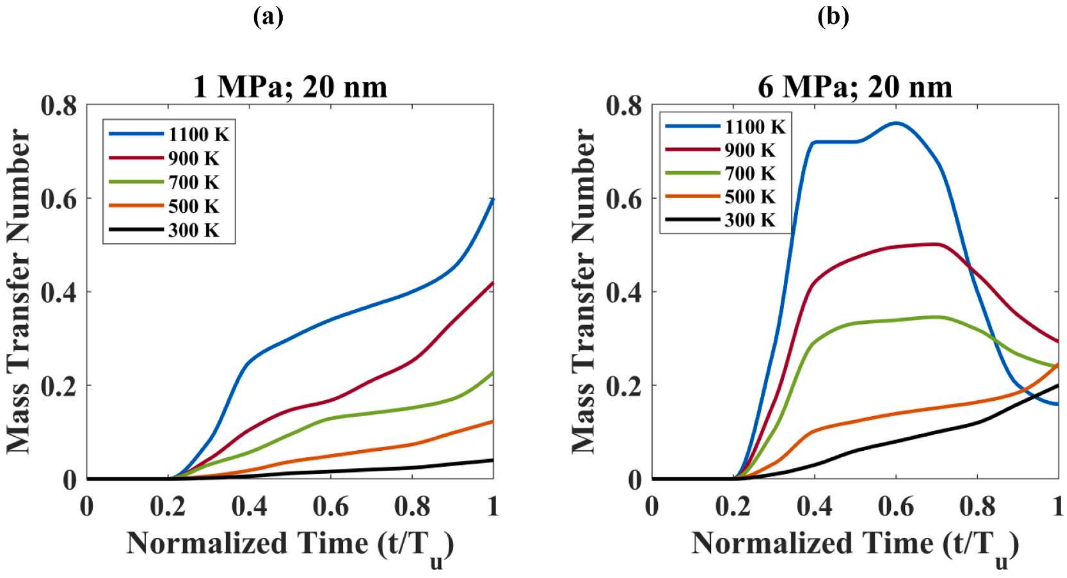

Fig. 20. Mass transfer number variation with temperature *vs.* normalized time t/T_u showing a difference in subcritical (1 MPa) and transcritical (6 MPa) cases for a 20 nm droplet diameter.

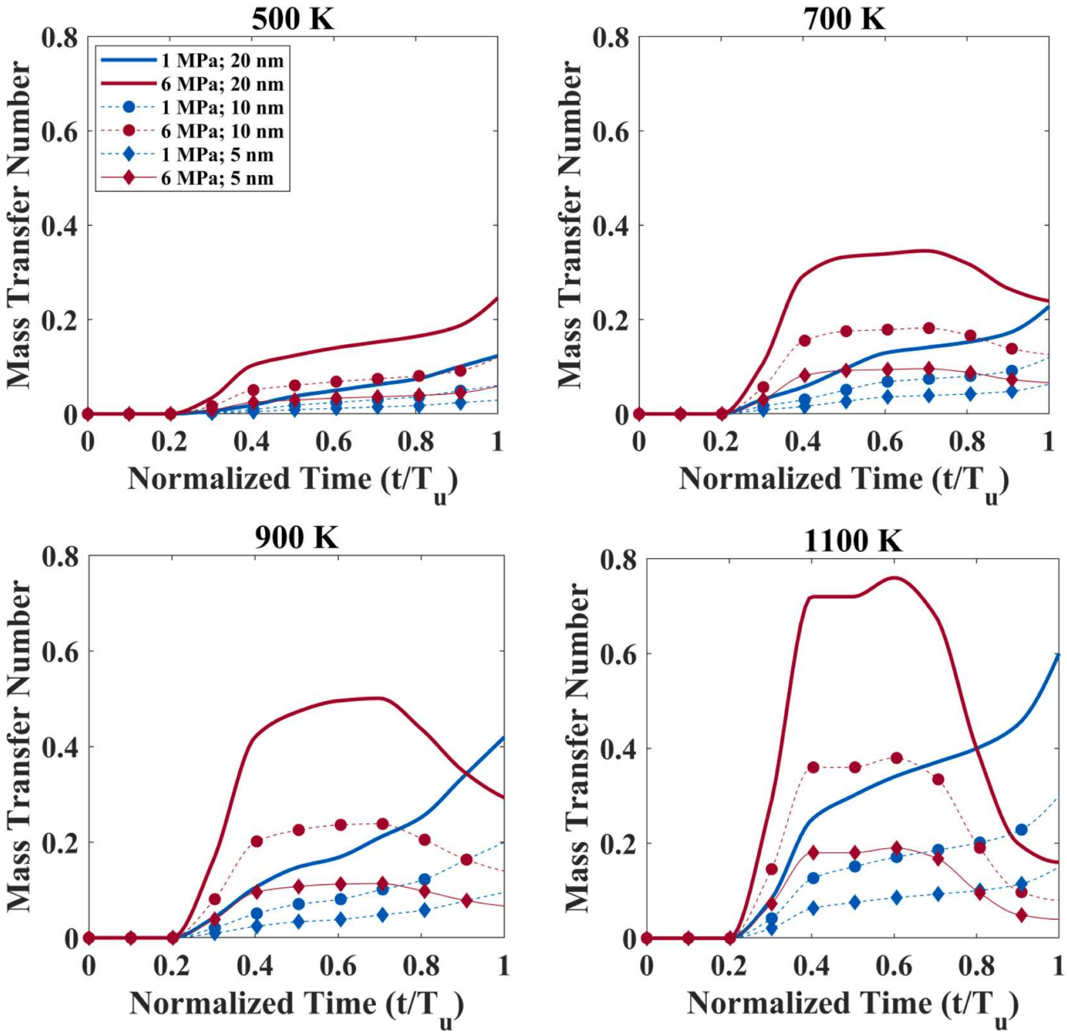

Fig. 21. Mass transfer number varies with pressure, temperature, and droplet size *vs.* normalized time with respect to the undroplet time, i.e., t/T_u.

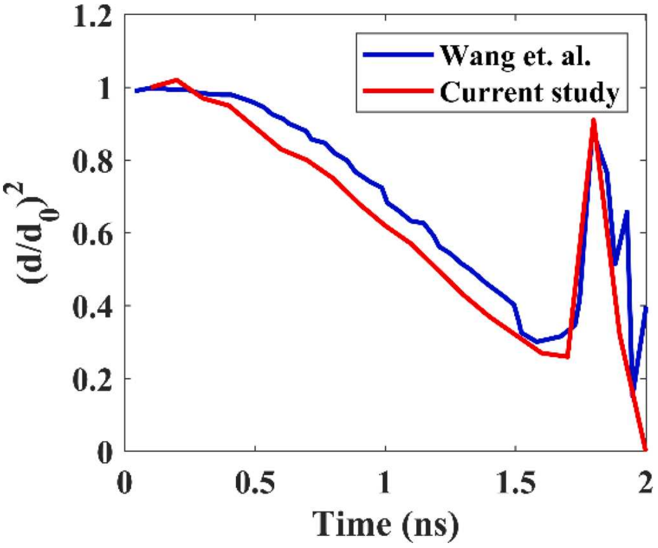

Fig. A1. Validation of the evaporation rate for a 15 nm-diameter n-dodecane droplet evaporating in nitrogen at 10.8 MPa and 1185 K compared with MD simulations conducted by Wang et al. [68].

4.6. Mass transfer number

To compare the effects of transcritical behavior on evaporation with its subcritical counterpart, the non-dimensional mass transfer number is defined as $B_m = \frac{Y_s - Y_\infty}{1 - Y_s}$, where Y_s is the mass fraction of *n*-dodecane vapor at the interface region including the thickened interface, and Y_∞ is the mass fraction of *n*-dodecane at the far-field region away from the droplet surface. The interface thickness is considered at the point where the local surface tension coefficient reaches a plateau, as shown in Fig. 7c. The number density of *n*-dodecane is calculated at the interface region and far-field based on MD results shown in Fig. 6 to calculate Y_s and Y_∞. Fig. 20 shows the variation of B_m with temperature *vs.* normalized time (t/T_u) at 1 and 6 MPa surrounding pressure for a 20 nm *n*-dodecane droplet to represent both sub- and supercritical conditions. As expected, the transcritical cases (700, 900, and 1100 K) at 6 MPa exhibit a peak in mass transfer during the interface thickening stage as a large number of atoms evaporate at the thickened interface before the droplet is entirely disintegrated. The peak of mass transfer number persists for a longer time at lower temperatures (700, 900 K at 6 MPa) and disappears before reaching the undroplet time. The mass transfer number increases by a factor of two during that period compared to the subcritical pressure case (i.e., 1 MPa). The mass transfer significantly drops, approaching the undroplet time as nitrogen penetrates the droplet core. The subcritical temperatures (300, 500 K) at 6 MPa and all cases at subcritical pressure of 1 MPa do not exhibit any peak even at supercritical temperatures, and the mass transfer increases monotonically since interface thickening does not occur at subcritical pressures.

Fig. 21 shows the variation of B_m with normalized time (t/T_u) for different temperatures, pressures, and droplet sizes. The increase in droplet size shows a proportionality with the mass transfer number, which is evident by a factor of two increases in the mass transfer peak with a two-fold increase in droplet size for transcritical cases. Fig. 21 also shows that for subcritical pressure of 1 MPa, the mass transfer does not exhibit a peak regardless of the droplet size and temperature. These results further highlight the uniqueness of transcritical evaporation reflected in the peak in mass transfer which occurs at supercritical pressures and temperatures close and above the critical temperature of *n*-dodecane due to interface thickening. A multiple regression model has been developed for the prediction of mass transfer number B_m, as shown in Equation (13), with an R^2 value of 0.76. The mass transfer number model has been developed based on the entire data set and can be used for sub- to supercritical conditions.

$$B_m = (1.59 \times 10^{-2}) p_b(MPa) + (2.15 \times 10^{-4}) T_b(K) + (1.32 \times 10^{-2}) d_0(nm) + (2.38 \times 10^{-1})(t/T_u) + (-3.98 \times 10^{-1}) \tag{13}$$

In summary, new models for surface tension coefficient, surface tension decay rate, evaporation rate, depleted mass, and mass transfer number for transcritical droplets are developed, which are applicable to a wide range of droplet sizes and background conditions. By normalizing the time with respect to the undroplet time, these models are independent of droplet size and weakly correlated with background pressure. Furthermore, a separate formulation for the undroplet time has been provided, which can be used in conjunction with the new models. Maximum and average absolute errors for multiple regression models have been provided in Appendix IV. Apart from multiple regression models that provide an explicit formulation for calculating surface tension and evaporation rate, the generated data using the gradient boosting model are stored and organized as Appendix B supplementary material submitted along with this paper. This library will enable readers to easily access the model and utilize the generated data without

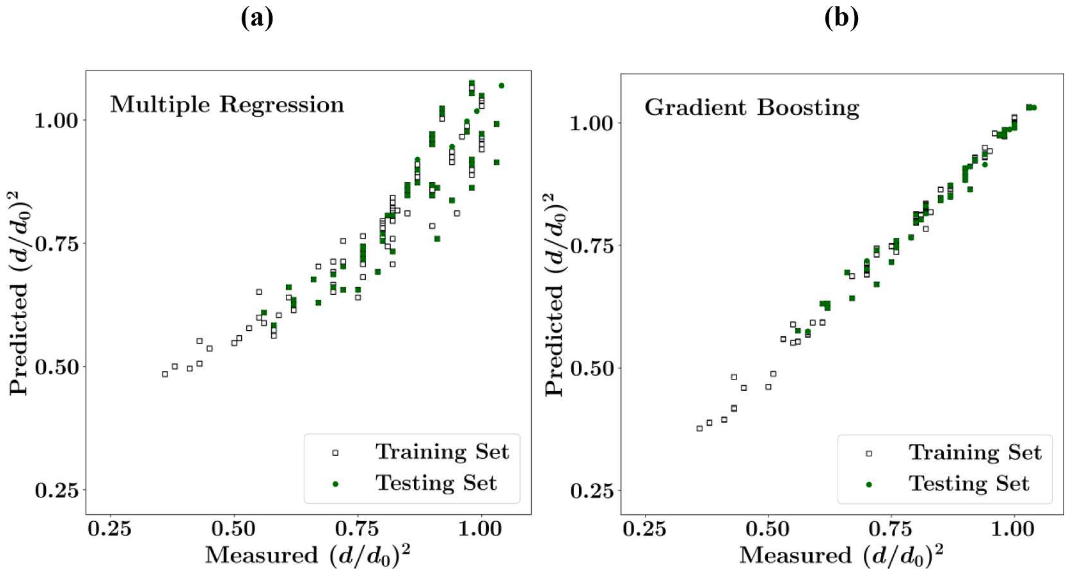

Fig. A2. Predicted evaporation rate $(d/d_0)^2$ *vs.* simulation using (a) multiple regression and (b) gradient-boosted tree ML methodologies.

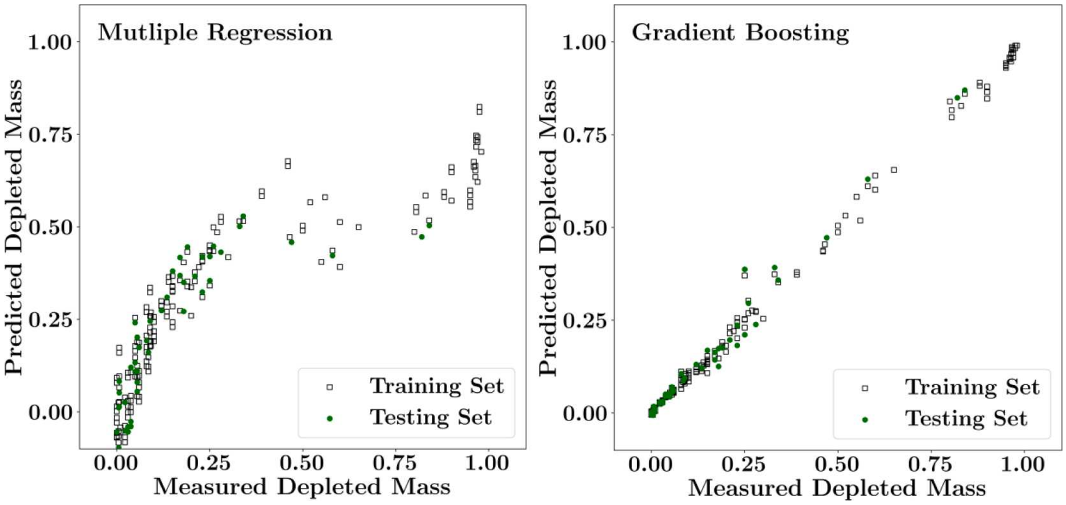

Fig. A3. Predicted normalized mass depletion (M/M_0)*vs.* simulation using (a) multiple-regression and (b) gradient boosted tree ML methodologies.

Table 5
Maximum and average error for multiple regression model.

Property	Maximum error	Average error
T_u	0.32 ns	0.11 ns
σ	2.31 mN/m	0.81 mN/m
$\dot{\sigma}$	3.12×10^8 N/ms	1.67×10^8 N/ms
$(d/d_0)^2$	0.18	0.11
M/M_0	0.24	0.16
B_m	0.14	0.09

having to retrain the machine learning model or replicate the data generation process. This library will promote reusability, code modularity, and efficiency of working with the generated data. Overall, these findings offer promising insights into the behavior of transcritical droplets, and the new models can be useful in practical applications. While the current study is focused on *n*-dodecane, which is of high interest to the combustion community, it is essential to investigate the effect of different hydrocarbons and multi-component hydrocarbon fuels and provide more accurate models for practical applications in high-pressure combustion systems. Therefore, in our future work, we plan to extend the current approach to investigate the transcritical behavior of other hydrocarbons and multi-component fuels.

5. Summary & conclusions

A comprehensive campaign of Molecular Dynamics simulations is conducted for an *n*-dodecane droplet with an initial subcritical temperature exposed to a nitrogen environment with pressure and temperature spanning from subcritical to supercritical conditions and different droplet sizes (total of 210 cases). Calculation of the surface tension coefficient using the Irving-Kirkwood method shows that phase transition from classical two-phase evaporation into a GL diffusion regime is strongly correlated with the decay of surface tension. A good agreement is observed between surface tension variation between current MD simulations and LGT theory. The evaporation rate is investigated by considering the changes in the droplet size and the rate of droplet mass depletion. To represent the surface tension and evaporation behavior at transcritical conditions, new models are developed by using multiple regression and gradient-boosted tree models. To find the pairwise correlation of independent variables, namely pressure, temperature, and droplet size with surface tension coefficient and evaporation rate, a correlation matrix is created based on the Pearson's product-moment correlation. The generated models are presented as correlation equations as well as online libraries in Appendix B supplementary materials accompanying this paper.

The following conclusions are drawn from the results:

1. Two key non-dimensional time parameters have been identified in this study: the first relates to the time required for the surface tension to completely vanish, while the second is associated with the moment when the nitrogen molecules reach the center of the droplet, known as the undroplet time which occurs after reaching zero surface tension.
2. The undroplet time exhibits a strong correlation with both the droplet size and the background temperature, with larger droplets requiring a longer time to undergo a complete transition to a GL state.
3. The results show that during the transcritical phase, the droplet exhibits liquid-like (LL) behavior with a decaying surface tension and a thickened interface where fuel and nitrogen interact, and the droplet core is intact. The transcritical phase is associated with a higher rate of evaporation by a factor of 2.5 compared to the initial phases of the evaporation.
4. Upon reaching the undroplet time, the droplet core undergoes disintegration, marking the transition to GL diffusion. This transition is accompanied by a significant increase in the evaporation rate, evident in the drastic expansion of the droplet and a fourfold increase in mass depletion.
5. The mass transfer number behavior further highlights the uniqueness of transcritical evaporation reflected in the mass transfer peak, which occurs only at supercritical pressures and temperatures close to and above the critical temperature of *n*-dodecane. This behavior is linked to the interface thickening behavior, where diffusion of the fuel as a GL fluid into nitrogen occurs within a thickened layer before the droplet is entirely disintegrated.
6. Pairwise correlation analyses reveal that normalizing the time with respect to the undroplet time yields surface tension coefficient, surface tension decay rate, and evaporation rate values that are independent of droplet size. Furthermore, it is observed that temperature exerts a more significant influence on these parameters compared to pressure.
7. This study provides new models for surface tension and evaporation rate independent of the droplet size that can be used in continuum simulations. These findings hold great promise for bridging the existing divide between nanoscale and microscale simulations of transcritical droplets.

Future work involves extending the presented analysis to understand the transcritical behavior of other hydrocarbons and multi-component fuels.

CRediT authorship contribution statement

Prajesh Jangale: Writing – original draft, Writing – review & editing, Software, Conceptualization. **Ehsan Hosseini:** Software. **Mohammad Zakertabrizi:** Software. **Dorrin Jarrahbashi:** Conceptualization, Writing – review & editing.

Declaration of competing interest

The authors declare the following financial interests/personal relationships which may be considered as potential competing interests: Dr. Dorrin Jarrahbashi reports financial support was provided by National Science Foundation.

Acknowledgements

This paper acknowledges the support received from the National Science Foundation, United States under Grant No #2237124. The authors express their gratitude to the High-Performance Research Computing (HPRC) resources at Texas A&M University for providing the necessary computational infrastructure to conduct the simulations.

Appendix I. Droplet evaporation rate validation

A cubic simulation box of size 75 nm with a 15 nm-diameter *n*-dodecane droplet, as shown in Fig. 2, is considered for validation of droplet evaporation rate compared to previous MD studies. The background nitrogen is set at 10.8 MPa pressure and 1185 K temperature, and the droplet is initially at a 363 K temperature. The simulation is run with the NVT ensemble for 1,000,000 steps with 2 fs time intervals and periodic boundary conditions in all directions. The fluid density in each grid is calculated by counting the number of atoms in the grid. The droplet interface boundary is defined where the calculated density is equal to the average of the maximum and minimum densities of the entire system, which is used as a reference point to calculate the instantaneous droplet diameter. To study the behavior of the droplet over time, the square of the non-dimensional droplet diameter $(d/d_0)^2$ is plotted versus time, where d_0 is the droplet initial diameter. The results show that during the quasi-steady evaporation period,$(d/d_0)^2$ decreases linearly with time. This behavior continues until the end of the evaporation phase, i.e., $t = 1.7$ ns, following an initial droplet heat-up period. An abnormal increase in droplet diameter is observed after 1.7 ns which indicates rapid diffusion of the *n*-dodecane molecules into nitrogen after reaching a GL state. The changes in the non-dimensional droplet radius with time, i.e.,$(d/d_0)^2$ is compared with the MD simulations of Wang et al. [68] as shown in Fig. A1. Slight differences observed in this figure are a result of different molecular structure setup for the *n*-dodecane molecules as Wang et al. [68] uses In contrast to the united-atom (UA) model, which treats CH_2— and CH_3— groups as a single force site, the current study employs an all-atom (AA) model where each atom is considered with its individual force site. This approach was chosen to enhance computational accuracy and capture finer details in the simulation.

Appendix II. Equations for radial distribution and mean squared displacement

Understanding the parameters of molecular dynamics simulations, we investigate the mean squared displacement Eqn. (A1), radial distribution function $g(\boldsymbol{r})$ Eqn. (A2) and the interaction energy given by the potential function in Equation (1). In Equation (A1), N is the number of molecules and $\boldsymbol{x}(t)$ is the location of a particular molecule at time t and reference time t_0. In Equation (A2), N_A and N_B are number of molecules of nitrogen and n-dodecane, and $\boldsymbol{r}$ gives the distance between neighboring molecules for the system. The variation of these properties for different temperatures shows that increasing temperature leads to larger mean squared displacements due to an increase in kinetic energy.

$$MSD = \left\langle \frac{1}{N} \sum_{1}^{N} \left| \overline{\boldsymbol{x}(t)} - \overline{\boldsymbol{x}(t_0)} \right|^2 \right\rangle_t \tag{A1}$$

$$g(r) = \frac{1}{N_A N_B} \sum_{i=1}^{N_A} \sum_{j=1}^{N_B} \left\langle \left| \boldsymbol{r}_i - \boldsymbol{r}_j \right| - r \right\rangle \tag{A2}$$

Appendix III. Agreement of data with the models

Predicted evaporation rate (Fig. A2) and normalized mass depletion (Fig. A3) with simulation using multiple regression and gradient-boosted tree ML methodologies. .

Appendix IV. Maximum and average error for multiple regression models

Table 5 shows the maximum and average error for multiple regression models for each of the predicted property.

Appendix B. Supplementary material

The library files are attached to the study. The files contain a gradient-boosting tree model trained as an XGBoost regression model using a dataset containing pressure, temperature, diameter, and normalized time. The model is trained to predict undroplet time, surface tension, surface tension rate, initial surface tension, evaporation rate: droplet diameter, normalized depleted mass, and mass transfer number based on the input parameters. The executable files are created and can be used to make predictions on new input parameters, such as pressure, temperature, diameter, and normalized time.

Supplementary data to this article can be found online at https://doi.org/10.1016/j.fuel.2023.130187.

References

[1] Hersch M, Rice EJ. Gaseous-hydrogen liquid-oxygen rocket combustion at supercritical chamber pressures; 1967.
[2] Oefelein JC. Thermophysical characteristics of shear-coaxial LOX–H2 flames at supercritical pressure. Proc Combust Inst 2005;30(2):2929–37.
[3] Harrje DT. Liquid propellant rocket combustion instability; 1972.
[4] Okong' N, Harstad K, Bellan J. Direct numerical simulations of O/H temporal mixing layers under supercritical conditions. AIAA J 2002;40(5):914–26.
[5] Miller RS, Harstad KG, Bellan J. Direct numerical simulations of supercritical fluid mixing layers applied to heptane–nitrogen. J Fluid Mech 2001;436:1–39.
[6] Miller R, Harstad K, Bellan J. Evaluation of equilibrium and non-equilibrium evaporation models for many-droplet gas-liquid flow simulations. Int J Multiph Flow 1998;24(6):1025–55.
[7] Bellan J. Supercritical (and subcritical) fluid behavior and modeling: drops, streams, shear and mixing layers, jets and sprays. Prog Energy Combust Sci 2000;26(4):329–66.
[8] Mayer H, et al. Atomization and breakup of cryogenic propellants under high-pressure subcritical and supercritical conditions. J Propul Power 1998;14(5):835–42.
[9] Zong N, Yang V. Cryogenic fluid jets and mixing layers in transcritical and supercritical environments. Combust Sci Technol 2006;178(1–3):193–227.
[10] Chehroudi B, Talley D, Coy E. Visual characteristics and initial growth rates of round cryogenic jets at subcritical and supercritical pressures. Phys Fluids 2002;14(2):850–61.
[11] Davis DW. On the behavior of a shear-coaxial jet, spanning sub-to supercritical pressures, with and without an externally imposed transverse acoustic field. Pennsylvania State Univ University Park Dept of Mechanical and Nuclear; 2006.
[12] Chehroudi BJIJAE. Recent experimental efforts on high-pressure supercritical injection for liquid rockets and their implications; 2012.
[13] Leyva I, Chehroudi B, Talley D. Dark core analysis of coaxial injectors at sub-, near-, and supercritical conditions in a transverse acoustic field. In: 43rd AIAA/ASME/SAE/ASEE joint propulsion conference & exhibit; 2007.
[14] Chehroudi B. Physical hypothesis for the combustion instability in cryogenic liquid rocket engines. J Propul Power 2010;26(6):1153–60.
[15] Oefelein J, Dahms R, Lacaze G. Detailed modeling and simulation of high-pressure fuel injection processes in diesel engines. SAE Int J Engines 2012;5(3):1410–9.
[16] Dahms RN et al. Understanding high-pressure gas-liquid interface phenomena in Diesel engines. Proc Combust Inst 2013;34(1):1667–75.
[17] Zhong F, et al. Heat transfer of aviation kerosene at supercritical conditions. J Thermophys Heat Transfer 2009;23(3):543–50.
[18] Sun F, et al. On assessment of heat transfer deterioration of a channel with supercritical n-decane for scramjet engines cooling. Int J Heat Mass Transf 2019;135:782–95.
[19] Jofre L, Urzay J. Transcritical diffuse-interface hydrodynamics of propellants in high-pressure combustors of chemical propulsion systems. Prog Energy Combust Sci 2021;82:100877.
[20] Wright SA et al. Operation and analysis of a supercritical CO2 Brayton cycle. Sandia Report, No. SAND2010-0171; 2010.
[21] Le Moullec Y. Conceptual study of a high efficiency coal-fired power plant with CO2 capture using a supercritical CO2 Brayton cycle. Energy 2013;49:32–46.
[22] Williams A. Combustion of droplets of liquid fuels: a review. Combust Flame 1973;21(1):1–31.
[23] Tarifa C, Crespo A, Fraga E. A theoretical model for the combustion of droplets in supercritical conditions and gas pockets. Astronautica Acta 1972:17.
[24] Sirignano W, Delplanque J-P. Transcritical vaporization of liquid fuels and propellants. J Propul Power 1999;15(6):896–902.
[25] Dahms RN. Understanding the breakdown of classic two-phase theory and spray atomization at engine-relevant conditions. Phys Fluids 2016;28(4):042108.
[26] Dahms RN, Oefelein JC. On the transition between two-phase and single-phase interface dynamics in multicomponent fluids at supercritical pressures. Phys Fluids 2013;25(9):092103.
[27] Chehroudi B et al. Understanding injection into high pressure supercritical environments. Air Force Research Lab Edwards AFB CA Propulsion Directorate; 2003.
[28] Chehroudi B. Recent experimental efforts on high-pressure supercritical injection for liquid rockets and their implications. Int J Aerosp Eng 2012;2012:1–31.
[29] Segal C, Polikhov SA. Subcritical to supercritical mixing. Phys Fluids 2008;20(5):052101.
[30] Poursadegh F, et al. On the fuel spray transition to dense fluid mixing at reciprocating engine conditions. Energy Fuel 2017;31(6):6445–54.
[31] Yang V, Shuen J-S. Vaporization of liquid oxygen (LOX) droplets in supercritical hydrogen environments. Combust Sci Technol 1994;97(4–6):247–70.
[32] Banuti DT. Crossing the Widom-line – supercritical pseudo-boiling. J Supercrit Fluids 2015;98:12–6.
[33] Mayer WOH, et al. Propellant atomization and ignition phenomena in liquid oxygen/gaseous hydrogen rocket combustors. J Propul Power 2001;17(4):794–9.
[34] Klima TC, Braeuer AS. Vapor-liquid-equilibria of fuel-nitrogen systems at engine-like conditions measured with Raman spectroscopy in micro capillaries. Fuel 2019;238:312–9.
[35] Gorokhovski M, Herrmann M. Modeling primary atomization. Annu Rev Fluid Mech 2008;40:343–66.
[36] Crua C, Manin J, Pickett LM. On the transcritical mixing of fuels at diesel engine conditions. Fuel 2017;208:535–48.
[37] Madana Gopal JV, et al. Understanding sub and supercritical cryogenic fluid dynamics in conditions relevant to novel ultra low emission engines. Energies 2020;13:3038.
[38] Mo G, Qiao L. A molecular dynamics investigation of n-alkanes vaporizing into nitrogen: transition from subcritical to supercritical. Combust Flame 2017;176:60–71.
[39] Dahms RN, Oefelein JC. Liquid jet breakup regimes at supercritical pressures. Combust Flame 2015;162(10):3648–57.
[40] Dahms RN, Oefelein JC. Non-equilibrium gas–liquid interface dynamics in high-pressure liquid injection systems. Proc Combust Inst 2015;35(2):1587–94.
[41] Dahms RN, Oefelein JC. Liquid jet breakup regimes at supercritical pressures. Combust Flame 2015;162(10):3648–57.
[42] Manin J, et al. Microscopic investigation of the atomization and mixing processes of diesel sprays injected into high pressure and temperature environments. Fuel 2014;134:531–43.
[43] Zuo Y-X, Stenby EH. A linear gradient theory model for calculating interfacial tensions of mixtures. J Colloid Interface Sci 1996;182(1):126–32.
[44] Poblador-Ibanez J, Sirignano WA. Transient behavior near liquid-gas interface at supercritical pressure. Int J Heat Mass Transf 2018;126:457–73.
[45] Dahms RN. Non-equilibrium gas-liquid interface dynamics in high-pressure liquid injection systems. Proc Combust Inst 2015;35(2):1587–94.
[46] Dahms RN, Pickett LM, Oefelein JC. Understanding high-pressure gasliquid interface phenomena in diesel engines. Proc Combust Inst 2013;34(1):1667–75.
[47] Nijmeijer MJP, et al. A molecular dynamics simulation of the Lennard-Jones liquid–vapor interface. J Chem Phys 1988;89(6):3789–92.
[48] Zhang Y et al. A molecular dynamics study of binary-component n-alkane fuel vaporization characteristics at sub/supercritical nitrogen environments. Proc Combust Inst 2021;38(2):3303–12.
[49] Matheis J, Hickel S. Multi-component vapor-liquid equilibrium model for LES of high-pressure fuel injection and application to ECN Spray A. Int J Multiph Flow 2018;99:294–311.
[50] Ma PC, Lv Y, Ihme M. An entropy-stable hybrid scheme for simulations of transcritical real-fluid flows. J Comput Phys 2017;340:330–57.
[51] Oefelein J, et al. Effects of real-fluid thermodynamics on high-pressure fuel injection processes. SAE Int J Engines 2014;7(3):1125–36.
[52] Poblador-Ibanez J, Sirignano WA. A volume-of-fluid method for variable-density, two-phase flows at supercritical pressure. Phys Fluids 2022;34(5).
[53] Poblador-Ibanez J, Sirignano WA. Temporal atomization of a transcritical liquid n-decane jet into oxygen. Int J Multiph Flow 2022;153:104130.
[54] Givler SD, Abraham J. Supercritical droplet vaporization and combustion studies. Prog Energy Combust Sci 1996;22(1):1–28.
[55] Qiu L, Reitz RD. An investigation of thermodynamic states during high-pressure fuel injection using equilibrium thermodynamics. Int J Multiph Flow 2015;72:24–38.
[56] Schmitt T, et al. Large-Eddy Simulation of transcritical flows. Comptes Rendus Mécanique 2009;337(6):528–38.
[57] Lapenna PE, Creta F. Mixing under transcritical conditions: an a-priori study using direct numerical simulation. J Supercrit Fluids 2017;128:263–78.
[58] Tani H, et al. A numerical study on a temporal mixing layer under transcritical conditions. Comput Fluids 2013;85:93–104.
[59] Boyd B, Jarrahbashi D. A diffuse-interface method for reducing spurious pressure oscillations in multicomponent transcritical flow simulations. Comput Fluids 2021;222:104924.
[60] Boyd B, Jarrahbashi D. Numerical study of the transcritical shock-droplet interaction. Phys Rev Fluids 2021;6(11):113601.
[61] Aggarwal SK, Yan C, Zhu G. Transcritical vaporization of a liquid fuel droplet in a supercritical ambient. Combust Sci Technol 2002;174(9):103–30.
[62] Beale JC, Reitz R. Modeling spray atomization with the Kelvin-Helmholtz/Rayleigh-Taylor hybrid model. Atomization Sprays 1999;9:623–50.
[63] Apte SV, Gorokhovski M, Moin P. LES of atomizing spray with stochastic modeling of secondary breakup. Int J Multiph Flow 2003;29(9):1503–22.
[64] Kaltz TL, et al. Supercritical vaporization of liquid oxygen droplets using molecular dynamics. Combust Sci Technol 1998;136(1–6):279–301.
[65] Xiao G, et al. A molecular dynamics study of fuel droplet evaporation in sub- and supercritical conditions. Proc Combust Inst 2019;37(3):3219–27.
[66] Gong Y, et al. A molecular dynamics study of evaporation mode transition of hydrocarbon fuels under supercritical conditions. Combust Flame 2022;246:112397.
[67] Gong Y, et al. Phase transitions of multi-component fuel droplets under sub- and supercritical conditions. Fuel 2021;287:119516.
[68] Wang Z, et al. Droplet evaporation and phase transition modes in supercritical environment by molecular dynamic simulation. Phys Fluids 2021;33(6):062001.
[69] Ly N, Majumdar A, Ihme M. Regimes of evaporation and mixing behaviors of nanodroplets at transcritical conditions. Fuel 2023;331:125870.
[70] He R, Yi P, Li T. Study on mechanism of abnormal variation of n-dodecane film thickness under supercritical condition by molecular dynamic simulations. Fuel 2023;331:125729.
[71] Chen C, Jiang X. Transport property prediction and inhomogeneity analysis of supercritical n-Dodecane by molecular dynamics simulation. Fuel 2019;244:48–60.
[72] Longmire NP, Showalter SL, Banuti DT. Holding water in a sieve—stable droplets without surface tension. Nat Commun 2023;14(1):3983.
[73] Poplow F. Numerical calculation of the transition from subcritical droplet evaporation to supercritical diffusion. Int J Heat Mass Transf 1994;37(3):485–92.
[74] Oefelein J, Aggarwal S. Toward a unified high-pressure drop model for spray simulations. Center for Turbulence Research; 2000.

[75] Oefelein JC, Yang V. Modeling high-pressure mixing and combustion processes in liquid rocket engines. J Propul Power 1998;14(5):843–57.
[76] Gaillard P, Giovangigli V, Matuszewski L. A diffuse interface Lox/hydrogen transcritical flame model. Combust Theor Model 2016;20(3):486–520.
[77] Zhu GS, Aggarwal SK. Transient supercritical droplet evaporation with emphasis on the effects of equation of state. Int J Heat Mass Transf 2000;43(7):1157–71.
[78] García-Córdova T, et al. Vapor–liquid equilibrium data for the nitrogen + dodecane system at temperatures from (344 to 593) K and at pressures up to 60 MPa. J Chem Eng Data 2011;56:1555–64.
[79] Yang V. Modeling of supercritical vaporization, mixing, and combustion processes in liquid-fueled propulsion systems. Proc Combust Inst 2000;28(1):925–42.
[80] Verlet L. Computer “Experiments” on classical fluids. I. Thermodynamical properties of Lennard-Jones molecules. Phys Rev 1967;159(1):98–103.
[81] Thompson AP, et al. LAMMPS - a flexible simulation tool for particle-based materials modeling at the atomic, meso, and continuum scales. Comput Phys Commun 2022;271:108171.
[82] Lennard-Jones JE. Cohesion. Proc Phys Soc 1931;43(5):461.
[83] Sun H. Ab initio calculations and force field development for computer simulation of polysilanes. Macromolecules 1995;28(3):701–12.
[84] Sun H, et al. An ab initio CFF93 all-atom force field for polycarbonates. J Am Chem Soc 1994;116(7):2978–87.
[85] Irving JH, Kirkwood JG. The statistical mechanical theory of transport processes. IV. The equations of hydrodynamics. J Chem Phys 1950;18(6):817–29.
[86] Bruneaux G, et al. Comparison of diesel spray combustion in different high-temperature, high-pressure facilities. SAE Int J Engines 2010;3(2):156–81.
[87] Walton JPRB, et al. The pressure tensor at the planar surface of a liquid. Mol Phys 1983;48(6):1357–68.
[88] Nomura H, et al. Microgravity experiments of fuel droplet evaporation in sub- and supercritical environments. Proc Combust Inst 2017;36(2):2425–32.
[89] Nomura H et al. Experimental study on high-pressure droplet evaporation using microgravity conditions; 1996.
[90] Friedman JH. Greedy function approximation: a gradient boosting machine. Ann Stat 2001;29(5):1189–232.
[91] Chen T, Guestrin C. Xgboost: a scalable tree boosting system. Proceedings of the 22nd ACM SIGKDD international conference on knowledge discovery and data mining. 2016.
[92] Bonett DG, Wright TA. Sample size requirements for estimating Pearson, Kendall and spearman correlations. Psychometrika 2000;65(1):23–8.
[93] Hauke J, Kossowski T. Comparison of values of Pearson’s and Spearman’s correlation coefficients on the same sets of data. Quaestiones Geographicae 2011;30(2):87–93.